Article

Cell Reports

3D Cellular Architecture Modulates Tyrosine Kinase Activity, Thereby Switching CD95-Mediated Apoptosis to Survival

Graphical Abstract

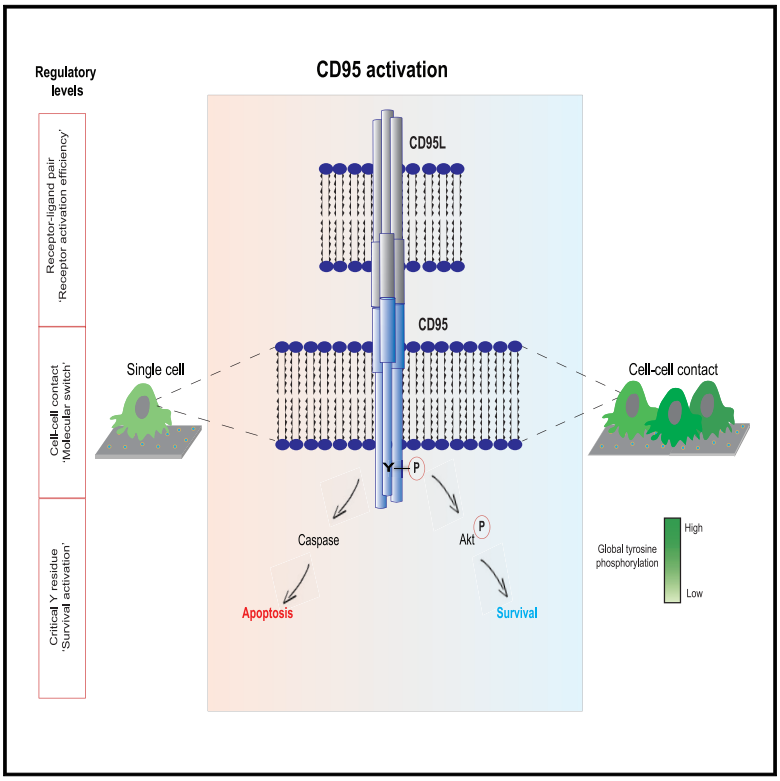

Authors

Gülce S. Gülcüler Balta, Cornelia Monzel, Susanne Kleber, ..., Yvonne Samstag, Motomu Tanaka, Ana Martin-Villalba

Correspondence

tanaka@uni-heidelberg.de (M.T.), a.martin-villalba@dkfz-heidelberg.de (A.M.-V.)

In Brief

Gülcüler Balta et al. show that CD95 receptor activation is determined through the presentation of its ligand at a certain intermolecular distance. The type of signaling triggered by CD95 is, however, decided by the cellular environment. CD95 triggers survival in cancer cells in contact with other cells and death in isolated ones.

Highlights

- Specific intermolecular spacing of CD95Ligand induces efficient CD95 clustering
- CD95 clustering triggers apoptotic and survival signaling
- CD95 signals survival in the presence of cell-cell contact
- Cell-cell contact increases levels of phosphotyrosinated proteins including CD95

Gülcüler Balta et al., 2019, Cell Reports *29*, 2295–2306
November 19, 2019
https://doi.org/10.1016/j.celrep.2019.10.054

CellPress

Cell Reports
Article

3D Cellular Architecture Modulates Tyrosine Kinase Activity, Thereby Switching CD95-Mediated Apoptosis to Survival

Gülce S. Gülcüler Balta,[1,2] Cornelia Monzel,[3,11] Susanne Kleber,[1] Joel Beaudouin,[5,6,12] Emre Balta,[7] Thomas Kaindl,[3] Si Chen,[1] Liang Gao,[1,13] Meinolf Thiemann,[8] Christian R. Wirtz,[9] Yvonne Samstag,[7] Motomu Tanaka,[3,10,*] and Ana Martin-Villalba[1,14,*]

[1]Department of Molecular Neurobiology, German Cancer Research Center (DFKZ), Im Neuenheimer Feld 581, 69120 Heidelberg, Germany
[2]Faculty of Biosciences, Heidelberg University, 69120 Heidelberg, Germany
[3]Physical Chemistry of Biosystems, Institute of Physical Chemistry, Heidelberg University, 69120 Heidelberg, Germany
[5]Department for Bioinformatics and Functional Genomics, Bioquant and Institute of Pharmacy and Molecular Biotechnology, Heidelberg University, 69120 Heidelberg, Germany
[6]Division of Theoretical Bioinformatics, German Cancer Research Center (DKFZ), Im Neuenheimer Feld 267, 69120 Heidelberg, Germany
[7]Section Molecular Immunology, Institute of Immunology, Heidelberg University, 69120 Heidelberg, Germany
[8]Apogenix AG, Im Neuenheimer Feld 584, 69120 Heidelberg, Germany
[9]Department of Neurosurgery, University Hospital Ulm, 89312 Günzburg, Germany
[10]Center for Integrative Medicine and Physics, Institute for Advanced Study, Kyoto University, 606-8501 Kyoto, Japan
[11]Present address: Experimental Medical Physics, Heinrich-Heine University Düsseldorf, 40225 Düsseldorf, Germany
[12]Present address: Institut de Biologie Structurale, Université Grenoble Alpes, Centre National de la Recherche Scientifique, Commissariat à l'Energie Atomique et aux Energies Alternatives, 38000 Grenoble, France
[13]Present address: The Brain Cognition and Brain Disease Institute, Shenzhen Institutes of Advanced Technology, Chinese Academy of Sciences, Shenzhen, China
[14]Lead Contact
*Correspondence: tanaka@uni-heidelberg.de (M.T.), a.martin-villalba@dkfz-heidelberg.de (A.M.-V.)
https://doi.org/10.1016/j.celrep.2019.10.054

SUMMARY

The death receptor CD95 is expressed in every cancer cell, thus providing a promising tool to target cancer. Activation of CD95 can, however, lead to apoptosis or proliferation. Yet the molecular determinants of CD95's mode of action remain unclear. Here, we identify an optimal distance between CD95Ligand molecules that enables specific clustering of receptor-ligand pairs, leading to efficient CD95 activation. Surprisingly, efficient CD95 activation leads to apoptosis in cancer cells *in vitro* and increased tumor growth *in vivo*. We show that allowing a 3D aggregation of cancer cells *in vitro* switches the apoptotic response to proliferation. Indeed, we demonstrate that the absence or presence of cell-cell contacts dictates the cell response to CD95. Cell contacts increase global levels of phosphorylated tyrosines, including CD95's tyrosine. A tyrosine-to-alanine CD95 mutant blocks proliferation in cells in contact. Our study sheds light into the regulatory mechanism of CD95 activation that can be further explored for anti-cancer therapies.

INTRODUCTION

Cancer is considered a disorder of signaling networks (Giancotti, 2014). Proliferation and survival of cancer cells are controlled by highly redundant signaling pathways that facilitate the development of resistance to molecular therapies (Sever and Brugge, 2015). Thus, therapies aimed at inducing cell death have a higher chance of avoiding resistance. The CD95 receptor represents an ideal candidate for targeted therapies, as it is expressed in every cancer cell and no loss-of-function mutations have been reported. Activation of CD95 in cancer cells may trigger apoptosis or tumorigenesis (Alderson et al., 1995; Brunner et al., 1995; Dhein et al., 1995; Ju et al., 1995). The activation of apoptosis by CD95 requires the assembly of a death-inducing signaling complex (DISC) composed of the adaptor protein Fas-associated protein with death domain (FADD) and the initiator Caspase-8 and −10. DISC assembly further activates other effector caspases in charge of cleaving cell substrates leading to the cell's own demise (Scott et al., 2009). On the other hand, CD95-mediated tumorigenesis has been linked to other signaling pathways, such as activation of nuclear factor κB (NF-κB), extracellular signal-regulated kinase (ERK), and phosphoinositide 3-kinase (PI3K) (Freiberg et al., 1997; Gulbins et al., 1998; Desbarats et al., 2003; Barnhart et al., 2004; Legembre et al., 2004; Kleber et al., 2008). Activation of kinase activities, such as ERK and PI3K, involves the recruitment of SH2-domain-containing proteins to a tyrosine residue within an

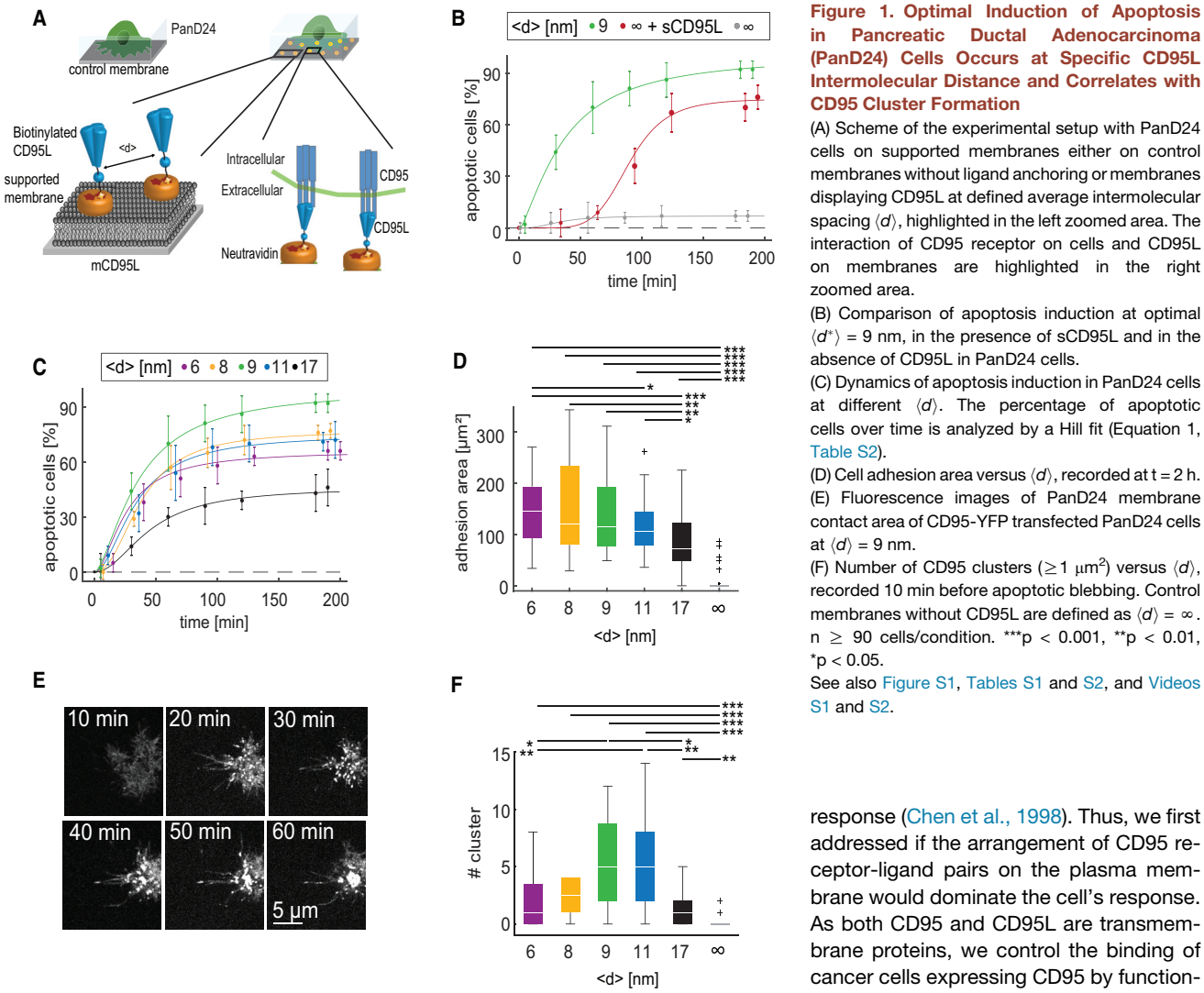

Figure 1. Optimal Induction of Apoptosis in Pancreatic Ductal Adenocarcinoma (PanD24) Cells Occurs at Specific CD95L Intermolecular Distance and Correlates with CD95 Cluster Formation

(A) Scheme of the experimental setup with PanD24 cells on supported membranes either on control membranes without ligand anchoring or membranes displaying CD95L at defined average intermolecular spacing $\langle d \rangle$, highlighted in the left zoomed area. The interaction of CD95 receptor on cells and CD95L on membranes are highlighted in the right zoomed area.

(B) Comparison of apoptosis induction at optimal $\langle d^* \rangle$ = 9 nm, in the presence of sCD95L and in the absence of CD95L in PanD24 cells.

(C) Dynamics of apoptosis induction in PanD24 cells at different $\langle d \rangle$. The percentage of apoptotic cells over time is analyzed by a Hill fit (Equation 1, Table S2).

(D) Cell adhesion area versus $\langle d \rangle$, recorded at t = 2 h.

(E) Fluorescence images of PanD24 membrane contact area of CD95-YFP transfected PanD24 cells at $\langle d \rangle$ = 9 nm.

(F) Number of CD95 clusters ($\geq$1 µm^2) versus $\langle d \rangle$, recorded 10 min before apoptotic blebbing. Control membranes without CD95L are defined as $\langle d \rangle = \infty$. n $\geq$ 90 cells/condition. ***p < 0.001, **p < 0.01, *p < 0.05.

See also Figure S1, Tables S1 and S2, and Videos S1 and S2.

immune receptor tyrosine-based inhibition/activation-like motif (ITAM/ITIM) in the death domain (DD) of CD95 to the PI3K-activating complex (PAC) (Atkinson et al., 1996; Daigle et al., 2002; reviewed in Sancho-Martinez and Martin-Villalba, 2009). Yet, how CD95 decides between the assembly of a DISC or a PAC is fundamentally not understood.

RESULTS

Optimal Induction of Apoptosis in Cancer Cells Occurs at Specific CD95L Intermolecular Distance and Correlates with CD95 Cluster Formation

The differential CD95 mode of action has been linked to activation of CD95 by a membrane-anchored CD95Ligand (mCD95L) or soluble CD95L (sCD95L), leading to activation of apoptosis or proliferation, respectively (Tanaka et al., 1995; Suda et al., 1997; Schneider et al., 1998; O' Reilly et al., 2009). However, forced expression of CD95L on cells has failed to fight the tumor but instead initiated a pro-tumorigenic inflammatory response (Chen et al., 1998). Thus, we first addressed if the arrangement of CD95 receptor-ligand pairs on the plasma membrane would dominate the cell's response. As both CD95 and CD95L are transmembrane proteins, we control the binding of cancer cells expressing CD95 by functionalizing a substrate with CD95L. To this end, we designed membrane-based surrogate surfaces (Tanaka and Sackmann, 2005; Burk et al., 2015) displaying the sCD95L fused to the T4-Foldon motif that was used as a trimerization domain (Figure 1A; Kleber et al., 2008). This membrane model system enables quantitative and precise control of the average intermolecular distance $\langle d \rangle$ between mCD95L on the membrane surface by changing the doping ratio of biotinylated lipid anchors (Table S1; see also STAR Methods for detailed explanation of $\langle d \rangle$ calculation). Cancer stem cells isolated from a pancreatic ductal adenocarcinoma patient (PanD24; Teodorczyk et al., 2015) were incubated with the mCD95L-supported membrane, and their apoptotic response was monitored over time by using label-free time-lapse microscopy. Using a ligand density of 13,200 ligands per µm^2, corresponding to $\langle d \rangle$ = 9 nm, we observed a rapid rise of the number of apoptotic cells, which reached 92% with a half time of 36 min (Figure 1B). In contrast, only 7% of apoptotic cells were observed on a membrane with no ligand, confirming that apoptosis results from specific CD95-mCD95L interactions. Moreover, the same ligand dissolved in solution (sCD95L; 1 µg/ml) also led to apoptosis.

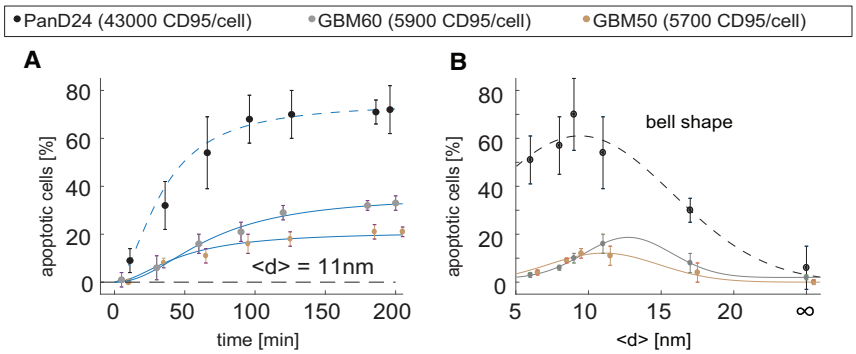

Figure 2. Apoptosis of Primary Cancer Cells Correlates with CD95 Expression Levels and Exhibits an Optimal CD95L Distribution as a Generic Signature

(A) Dynamics of glioblastoma (GBM) cell apoptosis at $\langle d \rangle$ = 11 nm.

(B) Percentage of apoptotic cells versus $\langle d \rangle$ (t = 1 h). Data of PanD24 at $\langle d \rangle$ = 11 nm are indicated as broken lines as reference. n $\geq$ 70 cells/condition. See also Tables S3 and S4.

The final level of sCD95L-mediated apoptosis reached 70%, but the kinetics was found to be much slower, showing a lag time of 40 min before an abrupt rise of the number of apoptotic cells. Characterization of the apoptotic dynamics using a Hill equation (see STAR methods for definition) revealed that sCD95L requires a longer lag time (Hill coefficient of n > 3) than mCD95L (Hill coefficient of $n \sim 1.5$).

This observation leads to the hypothesis that the confinement of CD95L on the membrane surface can activate the receptor efficiently and trigger rapid apoptosis. To further test this hypothesis, we measured the apoptotic response for different ligand densities, with an average $\langle d \rangle$ ranging from 6 to 17 nm (Table S1). Strikingly, the level of apoptosis did not increase proportionally with the decrease in $\langle d \rangle$ but showed the maximum efficiency of 92% at $\langle d \rangle \sim 9$ nm (Figure 1C; Table S2).

To further understand the functional role of $\langle d \rangle$ in apoptotic reactions, we first measured the adhesion area per cell as a function of $\langle d \rangle$ (Figure 1D) and found that the adhesion area does not take the maximum at $\langle d \rangle \sim 9$ nm but monotonically increases with decreasing $\langle d \rangle$. These data show that the CD95-mCD95L pairs anchor the cell to the surrogate surface, hence, increasing the cell's adhesion with increased engagement of ligand-receptor pairs, whereas efficient induction of apoptosis requires a specific arrangement of ligand-receptor interactions.

Moreover, by expressing yellow fluorescent protein (YFP)-tagged CD95 in PanD24, we observed the accumulation of the receptors in the adhesion zone (Figure 1E). YFP signals were diffusive during the early stage of cell spreading (Figure 1E; 10 min), followed by the formation of bright clusters over time (Video S1). On the other hand, YFP signal was homogenously distributed on control membranes, 1,2-dioleoyl-sn-glycero-3-phosphocholine (DOPC) (Video S2). The number of clusters measured 10 min before apoptosis took the maximum at $\langle d^* \rangle$ = 9–11 nm (Figure 1F). These data suggest that the surface displaying mCD95L at $\langle d^* \rangle$ enables the most efficient binding and clustering of ligand-receptor pairs, resulting in the strongest apoptotic signaling. The ligand-receptor pairing was also visualized by fluorophore-labeled neutravidin (NAV) and CD95-GFP expressing cells (Figure S1). Initially, homogeneous signals from NAV coupled to mCD95L exhibited a clear accumulation beneath the cell over time.

It should be noted that the density of ligands calculated from $\langle d^* \rangle$, 12,000 per μm^2, is three orders of magnitude larger than the density of CD95 on PanD24, namely, 13.4 per μm^2 (Table S3). Therefore, we hypothesized that the optimal ligand distance correlates with a critical molecular size of the receptors but not with the receptor density. To verify this point, we examined primary cancer cells originating from different glioblastoma multiforme (GBM) tumors (Drachsler et al., 2016). GBM60 and GBM50 cells were isolated from two different patients and both expressed 1.8 CD95 receptors per μm^2 (Table S3). With a ligand intermolecular distance of 11 nm, both cell lines exhibited apoptotic kinetics similar to PanD24 (Figure 2A). However, the final number of apoptotic cells was lower, with a plateau at around 35% for GBM60 and 21% for GBM50, which is 2–3 times lower than that of PanD24 (Figure 1C). Intriguingly, exactly as we observed for PanD24, we found that the surface displaying CD95L at $\langle d^* \rangle$ = 9–11 nm most effectively induced apoptosis in GBM cells (Figure 2B) with the smallest Hill coefficient (Table S4). Taken together, these data indicate the existence of an optimal CD95L spacing $\langle d^* \rangle$ = 9–11 nm to trigger apoptosis most efficiently across different cancer cell types.

Furthermore, to decipher whether the difference in signaling dynamics and efficiency stems from the lateral mobility of CD95-mCD95L pairs and their re-arrangement on the substrate, we used 1,2-dipalmitoyl-sn-glycero-3-phosphocholine (DPPC) membranes in which the lateral mobility of lipid molecules is significantly suppressed at 37°C (Gennis, 1989). On DPPC membranes displaying mCD95L, GBM50, and GBM60, cells died much slower than on DOPC (Figures 3A and 3E versus Figures 3B and 3F). However, the maximum levels of apoptotic cells after 6 h were comparable to those obtained on fluid DOPC membranes after 3 h. The distinctly slower kinetics of apoptosis can also be seen by a larger Hill coefficient on DPPC (n = 3–6; Table S4) with respect to DOPC membranes (n = 1.7–4; Table S4). Accordingly, the formation of CD95 clusters was significantly suppressed (Figures 3C and 3G and Figures 3D and 3H), indicating that loss of membrane fluidity suppressed the formation of death-inducing clusters.

mCD95L-Supported Membrane-Coated Beads Promote Tumor Growth

So far, our data show that CD95L pre-confined at an optimal intermolecular distance can effectively trigger CD95-mediated apoptosis in cancer cells *in vitro*. Thus, we hypothesized that this knowledge could be used to efficiently kill tumor cells *in vivo*. To this end, we assembled latex beads coated with supported membranes displaying CD95L at $\langle d^* \rangle$ = 9 nm and compared

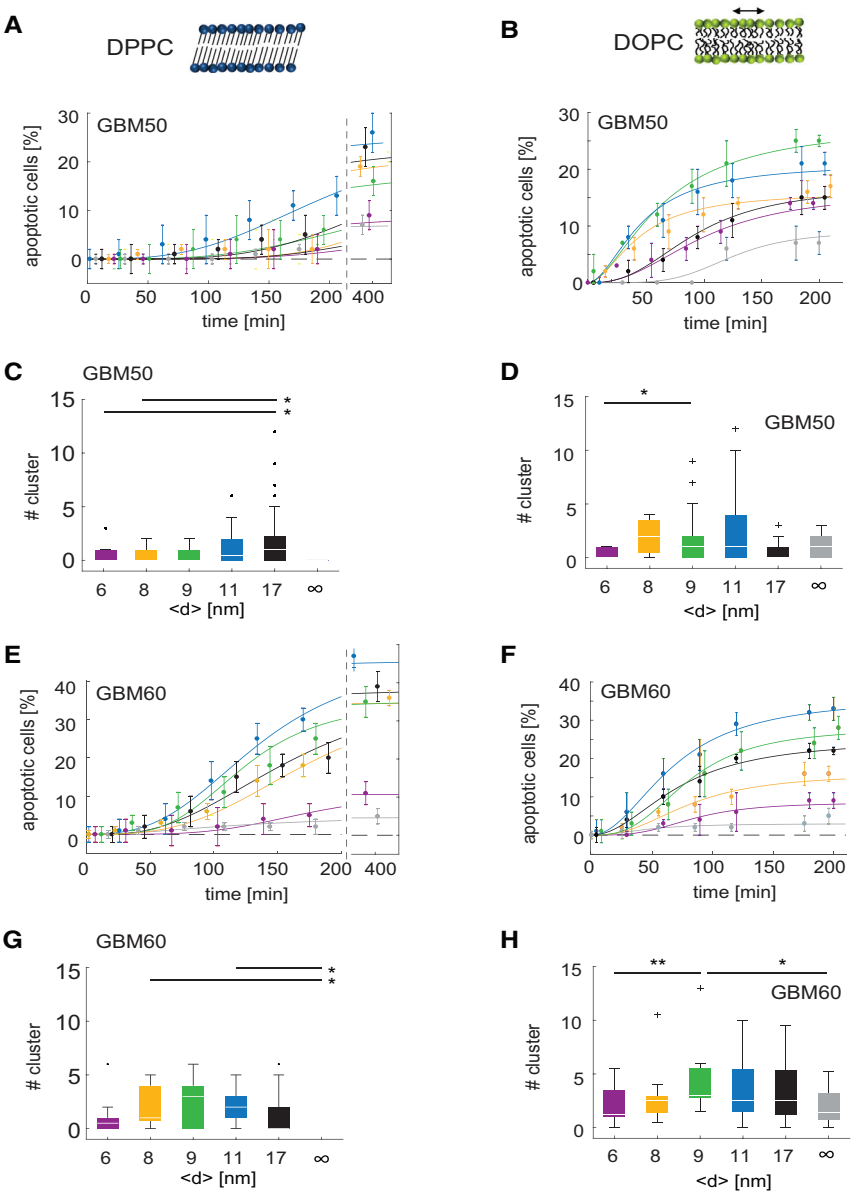

Figure 3. Lateral Mobility of Lipids on Supported Membrane Impacts the Apoptosis Induction and CD95 Receptor Clustering.

Inhibition of CD95L mobility by DPPC-supported membranes results in slowdown of apoptosis induction (A and E) and supression of CD95 cluster formaion (C and G). Apoptosis induction in GBM cells is optimal at specific CD95L intermolecular distances on DOPC-supported membranes (B and F) and correlates with CD95 cluster formation (D and H).

(A and E) Dynamics of apoptosis induction in GBM50 (A) and GBM60 (E) cells at different $\langle d \rangle$ on DPPC. The percentage of apoptotic cells over time is fitted with a Hill function (Equation 1, see Table S4 and text for fit results).

(C and G) Number of CD95 clusters for GBM50 (C) and for GBM60 (G) on DPPC-supported membranes at different $\langle d \rangle$. Clusters are $\geq 1\ \mu m^2$, and their number is analyzed 10 min before cell blebbing/apoptosis.

(B and F) Dynamics of apoptosis induction in GBM50 (B) and GBM60 (F) cells at different $\langle d \rangle$ on DOPC (see Table S4 and text for fit results).

(D and H) Number of CD95 clusters for GBM50 (D) and for GBM60 (H) on DOPC supported membranes at different $\langle d \rangle$. n $\geq$ 40 cells/condition. ***p < 0.001, **p < 0.01, *p < 0.05.

See also Table S4.

with the beads coated with pure DOPC membranes (Figure 4A). Then, tumor cells were subcutaneously (s.c.) injected into the flanks of immunosuppressed SCID^{bg} mice (Figure 4A). The s.c. location was selected over the brain to avoid beads having to cross the blood-brain barrier to reach the tumor. To control for effects arising from activation of CD95 in non-tumor cells, we injected either CD95^{high}, CD95^{low} (sorted as previously described in Drachsler et al., 2016), or unsorted (bulk) GBM cells. Three weeks after cell injection, tumors were already detected and, hence, this time was chosen for intravenous (i.v.) bead injection. Thereafter, tumor growth was further monitored. To our surprise, instead of the expected reduction in tumor size, treatment with CD95L beads exponentially increased growth of bulk or CD95^{high} tumors. This increase in tumor growth was not present in the CD95^{low} tumors or tumors treated with control beads, indicating that the proliferative effect was directly driven by CD95 on tumor cells (Figure 4B). Thus, inflammatory cells or vessels could be excluded as the main drivers of this pro-tumorigenic effect. Furthermore, the same CD95-dependent tumor growth was observed in xenograft tumors derived from another GBM patient (Figure S2A). Of note, control CD95^{high} tumors showed a lack of tumor growth in the first patient (Figure 4B) that we never observed in CD95^{high} tumors of other patients (Figure S2A; Drachsler et al., 2016). Such behavior might indicate a higher dependency of this patient's tumor cells on CD95L. The beads could be detected in several locations, such as the tumor, lung, and liver, showing no signs of apoptosis in lung and liver (Figures S2B and S2C). This finding demonstrates that beads coated with mCD95L at the optimal distance foster proliferation of tumor cells directly acting by CD95 on these cells *in vivo*.

To gain further mechanistic insights into the determinants of the pro-tumorigenic response mode to CD95, we used a syngeneic orthotopic glioma model (Figure S3A). This model additionally allows study of the cell's response to CD95 in the natural environment of the brain in the background of a fully competent immune system. To this end, cells derived from a spontaneous murine astrocytoma (SMA560) were intracranially (i.c.) injected into the striatum of VMDK mice. Five days post tumor cell implantation, the beads coated with membranes displaying CD95L at $\langle d \rangle$ = 8 nm compared with the control beads coated

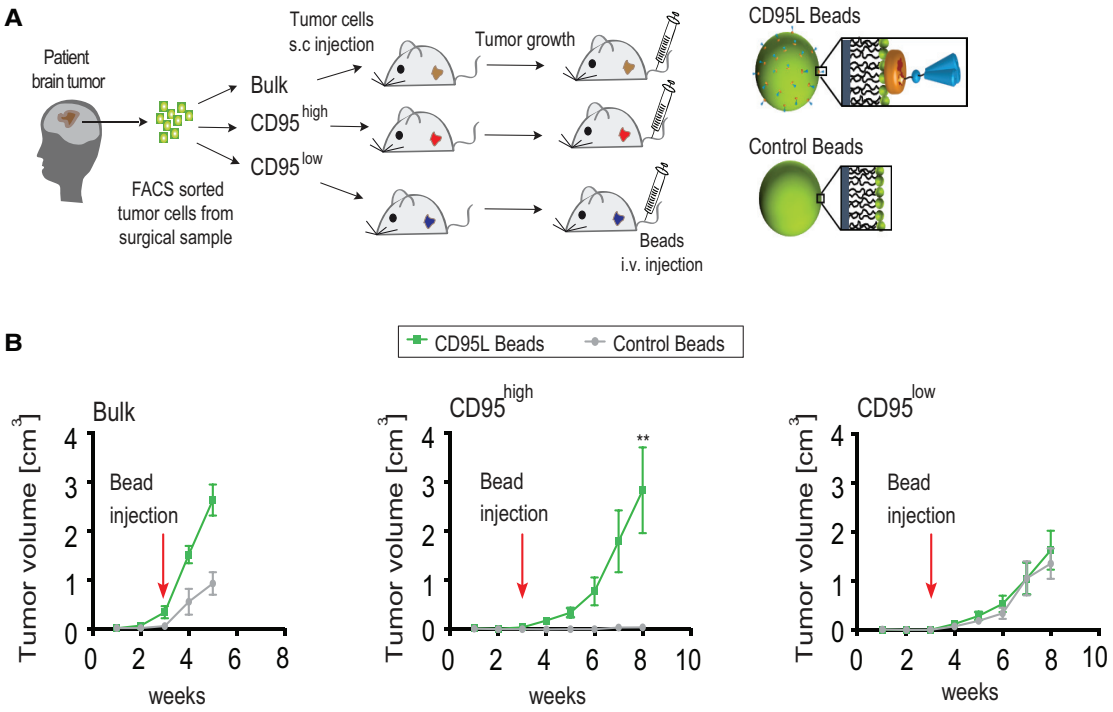

Figure 4. CD95L-Coated Beads Promote Subcutaneous Tumor Growth

(A) Scheme of the patient-derived tumor xenograft model (GBM39). Cancer cells are fluorescence-activated cell sorting (FACS)-sorted according to CD95 surface expression levels and grown in mice subcutaneously before the intravenous (i.v.) injection of the beads. Either non-functionalized DOPC-membrane-coated beads (control beads) or CD95L functionalized beads were injected.

(B) Kinetics of tumor progression upon bead injection (control beads = gray data, n = 3; CD95L beads = green data, n = 4–5). CD95L distance on beads $\langle d \rangle$ = 9 nm. Values are mean ± SEM; two-way ANOVA, **p < 0.0013.

See also Figure S2 and S3.

with pure lipid membranes were injected i.c. The mice were sacrificed once the maximum tolerable tumor volume was reached. Thereafter, brain tumor sections were stained for phospho-ERK (p-ERK), phospho-Histone3 (p-H3), cleaved Caspase-3, and phospho-Akt (p-Akt) (Figure S3B). The number of cells positive for p-ERK and p-Akt were significantly higher in tumors exposed to CD95L beads, compared to control-bead-treated tumors (Figure S3C). This is in line with previous studies demonstrating that the pro-tumorigenic CD95-signaling cascade involves activation of the ERK and/or PI3K signaling pathways (Kleber et al., 2008; Martin-Villalba et al., 2013; Teodorczyk et al., 2015). A clear increase in the mitotic index of tumors treated with CD95L beads compared to control beads was assessed by p-H3 staining (Figures S3B and S3C). On the other hand, there was no difference in the number of cells undergoing apoptosis between the two groups, as assessed by staining of cleaved Caspase-3 (Figures S3B and S3C). Based on these data, we concluded that CD95-dependent proliferation of cancer cells highly correlates with increased activation of Ras/ERK and PI3K signaling pathways.

Presence of Cell-Cell Contact Switches the Apoptotic Response to Proliferation

What is the origin of these antithetic cellular responses observed *in vivo* and *in vitro*? One apparent difference is that the cells *in vivo* were immersed in the multicellular network of three-dimensional tumors, whereas the *in vitro* experiments were performed using isolated single cells on planar surfaces. To test if the different cell responses originate from cell-cell interactions, we investigated the functional outcome of mCD95L stimulation of cancer stem cells within three-dimensional tumorspheres *in vitro*. The self-renewal was assessed by counting the number of tumorspheres as a function of $\langle d \rangle$. Surprisingly, also *in vitro*, exposure of tumorspheres to mCD95L-supported membranes triggered a significant increase of self-renewal (Figure 5A) instead of apoptosis (Figure 5B). Importantly, the maximum sphere number (38 ± 3) was found at the optimal distance $\langle d^* \rangle$ (Figure 5A). Similar behavior was also observed in PanD24 tumorspheres, while the highest number of spheres was detected at $\langle d \rangle$ = 17 nm (Figure S4A). Based on our data, we concluded that the confinement of CD95L at $\langle d^* \rangle$ enhanced the self-renewal most efficiently in solid tumors *in vivo* and tumorspheres *in vitro*. To test the physiological relevance of the identified optimal distance and the presence of cell-cell contact, we turned to a non-neoplastic cell system of cells that are naturally in contact with each other. We have previously shown that activation of CD95 on myeloid cells enhances their rolling and adhesive behavior, facilitating recruitment to the inflammatory site (Gao et al., 2016). Accordingly, mouse bone-marrow-derived neutrophils increased integrin activation as assessed by a ICAM1 binding

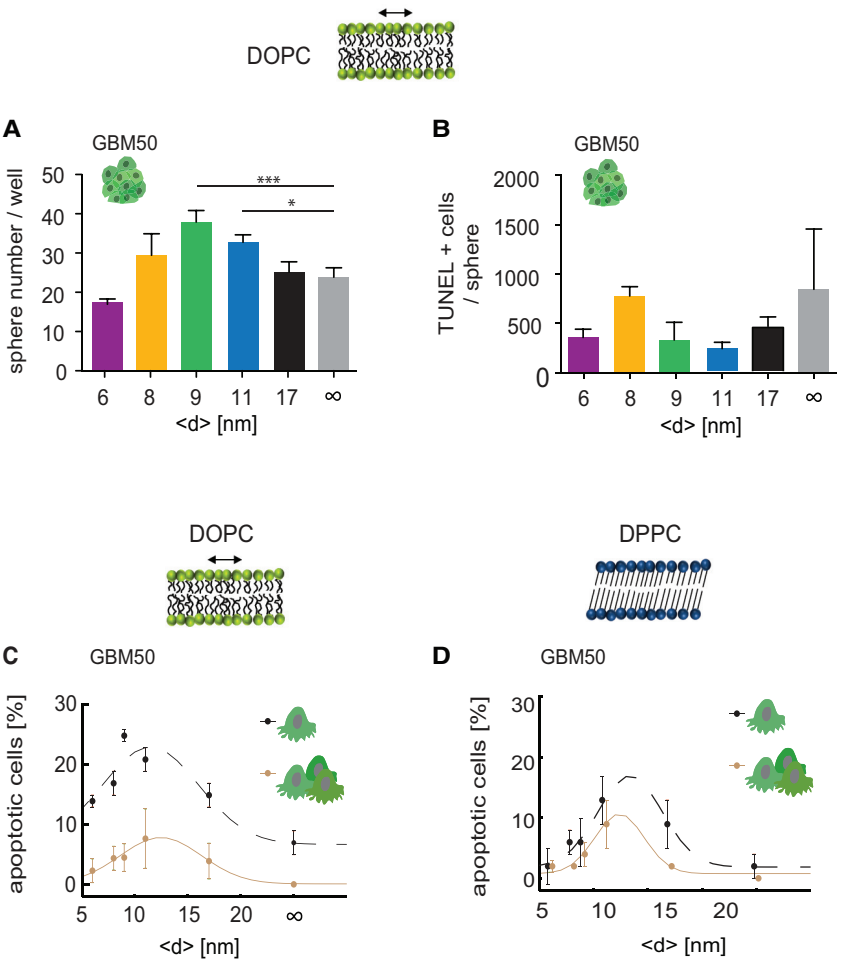

Figure 5. CD95 Activation Enhances Self-Renewal Capacity of Tumorspheres

(A) Patient-derived glioma sphere cultures (GBM50) were treated for 4 h with CD95L-coated membranes and were subsequently plated for sphere formation assessment. Values are mean ± SEM.; one-way ANOVA, *$p < 0.02$, ***$p < 0.0002$.

(B) TUNEL assay for GBM50 tumorspheres was performed to assess apoptotic cells after 4-h treatment with CD95L-coated membranes. Values are mean ± SEM.

(C and D) Apoptotic behavior of GBM50 in contact with other cells on DOPC (C) and DPPC (D) membranes functionalized with CD95L at different $\langle d \rangle$ was analyzed at t = 200 min. Broken line: data of isolated individuals. $n \geq 40$ cells/condition. Values are median ± median absolute deviation (MAD).

See also Figures S4 and S5 and Videos S3, S4, and S5.

assay. Now, we show that neutrophils increased ICAM-1 binding upon mCD95L stimulation at a specific intermolecular distance ($\langle d \rangle$ = 11–17 nm) (Figure S4B). In addition, we have previously shown that CD95 activation of endothelial cells controls vessel branching in the developing cortex and retina (Chen et al., 2017a). Therefore, we exposed human endothelial cells (HUVECs) to mCD95L at different intermolecular distances of CD95L (Figure S4C). Indeed, only mCD95L presented at the optimal intermolecular distance increased angiogenic activity but not apoptosis of HUVECs (Figures S4D–S4G). Thus, a unique intermolecular distance controls CD95's activation mode in neoplastic and healthy cells.

Next, we addressed if the presence of merely one or two cell-cell contacts would be enough to shift the response of the cell to CD95 activation away from apoptosis. Therefore, we monitored and compared apoptosis of GBM50 cells either exhibiting up to two cell-cell contacts or as isolated cells on the same supported membranes (Figure 5C; Video S3). GBM cells in contact with other cells exhibited a distinct lower fraction of apoptosis induction (reduction by ~2-fold) for all $\langle d \rangle$ conditions compared to isolated cells. Moreover, the cells from other GBM patients, as well as HeLa cells from another cancer type (cervical cancer) showed lower apoptosis when they are in contact with other cells (Figures S5A and S5B, broken lines). With this knowledge, we hypothesized that the difference in final number of apoptotic cells between PanD24 cells (92%) and GBM cells (21%–35%) could be due to differences in their tendency to form clusters with neighboring cells. To validate this hypothesis, we analyzed the cohesive behavior of these cells on the mCD95L membranes. GBM cells were highly mobile and showed a high tendency to adhere to neighboring cells by forming protrusions leading to the establishment of cell-cell contacts (Figure S5C; Video S4). However, PanD24 cells did not exhibit a pronounced cell motion but remained attached to the mCD95L-coated membrane (Figure S5D; Video S5). In both cell types, apoptosis induction of single cells was observed while examples of cell divisions were found in the presence of cell-cell contacts. In summary, in solid tissues where cells are in contact with neighboring cells, CD95 activation promotes pro-survival signaling, whereas the loss of cell-cell contact renders CD95-stimulated cells sensitive to undergo apoptosis. Notably, the same tendency was observed on DPPC membranes (Figure 5D; Figures S5E and S5F), suggesting the bifurcation between apoptosis and proliferation does not depend on the mobility of CD95L molecules. The obtained results suggest that the apoptosis kinetics is strongly influenced by intermolecular distance between CD95L $\langle d \rangle$ and the lateral mobility of CD95L, whereas the mode of cellular response, i.e., apoptosis versus proliferation, is determined by the presence or absence of cell-cell contacts.

Cell-Cell Contact Increases Global Tyrosine Kinase Activity That Is Required for CD95 Activation-Induced Self-Renewal of Tumorspheres

How does cell-cell contact influence the cell response to CD95 activation? It has been shown that signaling of apoptosis requires

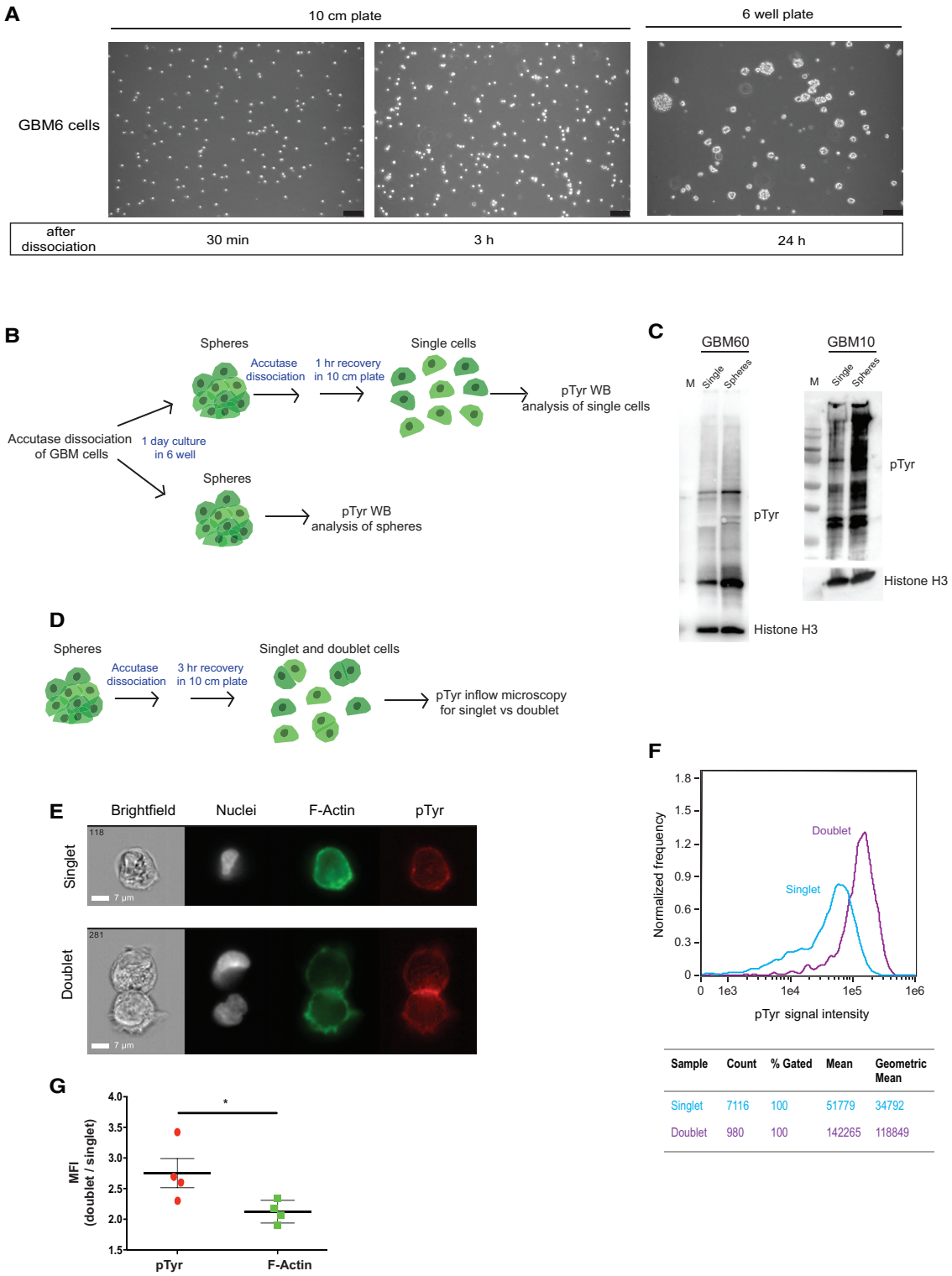

Figure 6. Cell-Cell Contact Increases Global Tyrosine Kinase Activity

(A) Representative images of GBM6 single cells, doublets in 10-cm plate, and spheres in 6-well plate format are shown. The cells were seeded at 0.5×10^6 cell density; time after accutase dissociation is indicated below the images. Scale bar, 50 µm.

(B) Experimental setup for western blot analysis of single versus spheres.

(legend continued on next page)

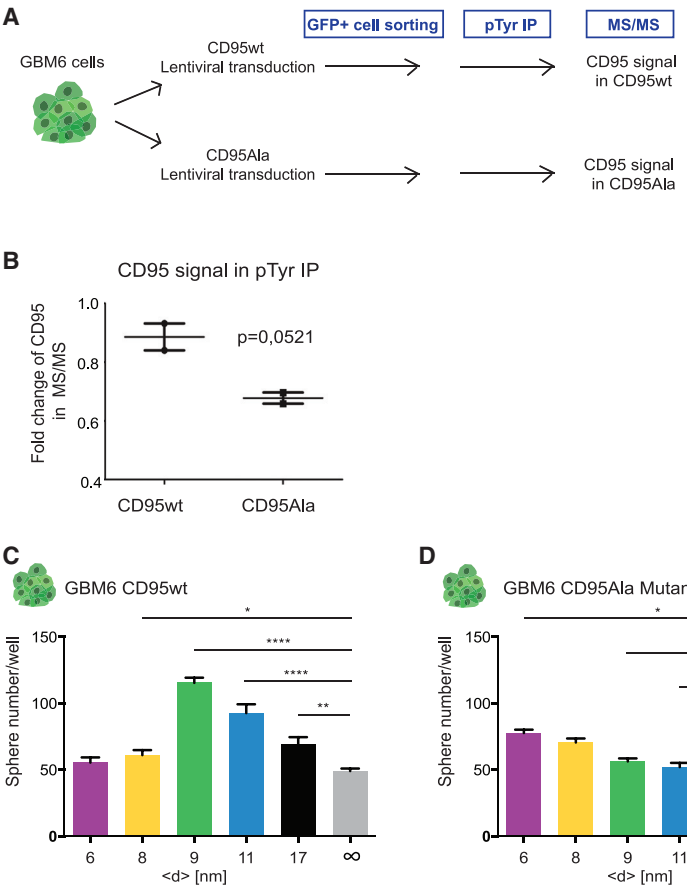

Figure 7. CD95 Tyrosine Phosphorylation Is Increased in Spheres and Is Required for CD95-Activation-Induced Self-Renewal of Tumorspheres

(A) Experimental setup for mass spectrometry analysis of pTyr immunoprecipitation (pTyr IP) samples from CD95-WT or CD95-Ala-overexpressing cells.

(B) Normalized CD95 signal (LFQ) was detected by MS/MS from pTyr IP samples either CD95-WT or CD95-Ala-overexpressing tumorspheres (GBM6) treated with CD95L antibody (Apo-1) for 5 min. The fold change was calculated from the ratio of CD95 signal in IP over flow through (FT) for each sample (n = 2).

(C and D) CD95-WT (C) overexpressing or CD95-Ala (D) mutant overexpressing glioma cells (GBM6) were treated as spheres for 4 h on CD95L-coated membranes at different ⟨*d*⟩. Subsequently, they were plated to measure the sphere-forming capacity. Values are mean ± SEM; t test, *p < 0.05; **p < 0.01; ****p < 0.0001. n = 3.

See also Figure S7.

the recruitment of DISC to CD95 DD, whereas proliferation involves phosphorylation of residue Y291 located within the DD (Kleber et al., 2008; Chakrabandhu et al., 2016; Drachsler et al., 2016). In light of this knowledge, we hypothesized that cell-cell contact might favor tyrosine phosphorylation over DISC assembly. First, we defined the cell plating settings to obtain single cells, doublets, and spheres (Figure 6A). Indeed, the presence of cell-cell contact globally increased the levels of tyrosine-phosphorylated proteins compared to levels exhibited in single cells, as detected with a generic anti-phosphotyrosine (pTyr) antibody (Figures 6B and 6C). Next, we investigated global pTyr levels in naturally occurring single cells and doublet cells by imaging flow cytometry (Figures 6D and 6E; see Figures S6A and S6B for more representative images of cells and Figures S6C–S6F for experimental settings). This method allowed us to discriminate singlet and doublet cells and image ~10,000 cells per sample. Thereafter, we performed control experiments for pTyr staining after a physiological stimulus, epidermal growth factor (EGF), or after a phosphatase inhibitor, vanadate treatment (Figures S6G and S6H). Upon these treatments, global pTyr levels were also increased, and importantly the highest level was reached by vanadate treatment (Figure S6H). Similar to western blot results, the levels of pTyr per cell were much higher in doublets (2.753 ± 0.237 fold-change, n = 4) than in single cells compared to the actin signal (2.124 ± 0.093 fold-change, n = 4) (Figures 6F and 6G). Thus, we conclude that the presence of cell-cell contact increases global levels of tyrosine kinase activity.

To confirm the importance of phosphorylation of the tyrosine motif in CD95-mediated proliferation, we generated GBM6 cells stably overexpressing either wild-type CD95 (CD95-WT) or CD95-alanine mutant (CD95-Ala) that substitutes the Y291 residue of the human CD95 by alanine (Figure 7A). We detected CD95 within the pool of phosphorylated proteins obtained from pTyr immunoprecipitation (IP) and analyzed by liquid chromatography-tandem mass spectrometry (LC-MS/MS). The quantified CD95 signal was lower in CD95-Ala expressing tumorspheres than CD95-WT cells (Figure 7B). Of note, the total number of identified peptides and proteins were similar in all samples (Figures S7A and S7B). Consistently, the control proteins containing pTyr sites irrelevant to CD95 signaling were enriched at a similar

(C) Western blot analysis of single cells versus spheres from GBM60 and GBM10, probed for pTyr antibody. Same membranes were incubated with anti-Histone H3 antibody for loading control.

(D) Experimental setup for imaging flow cytometry analysis of single cells versus doublets.

(E) Examples of inflow microscopy images of nuclei (DAPI), pTyr-PE, and F-actin (AF488) in singlet versus doublet. Scale bar, 7 μm. A 60× objective was used.

(F) A representative histogram and quantification of pTyr signal in singlet versus doublets by imaging flow cytometry.

(G) Geometric mean fluorescence intensity (MFI) from doublet/singlet gates were plotted for pTyr and F-actin signals. 10,000–20,000 cells per sample were analyzed (n = 4). Values are mean ± SEM. t test, *p < 0.05.

See also Figure S6.

level in the IP samples (Figures S7C and S7D). Upon exposure of these cells to CD95L surrogate membranes, the self-renewal capacity of the CD95-Ala cells was significantly impaired compared to the CD95-WT cells (Figures 7C and 7D). These data highlight the critical regulation of survival at the DD of CD95 and the requirement of tyrosine kinase activity to drive the cell response to CD95 toward activation of proliferation signals.

DISCUSSION

In this study, we unveil two levels at which CD95-mediated signaling is controlled. First, the optimal arrangement of receptor-ligand pairs on the surface of plasma membranes controls the receptor-activation efficiency. Second, the cell-cell contacts increase the tyrosine phosphorylation globally, thereby deciding whether the cell undergoes apoptosis or rather activates a survival program.

We have established membrane-based surrogate cell surfaces displaying mCD95L to study CD95 activation in cancer cells. This system revealed an optimal mCD95L intermolecular distance as the most efficient to trigger CD95 cluster formation and, thereby, apoptosis in primary cancer cells *in vitro*. In particular, the reconstitution of mCD95L on the supported membrane at an intermolecular distance $\langle d^* \rangle$ = 9–11 nm was found to maximize the efficiency and kinetics of receptor activation. In addition to cancer cells, endothelial cells and myeloid cells selectively respond to this "optimal intermolecular distance" of CD95L with an angiogenesis or integrin activation, respectively. Thus, suggesting the selective activation of CD95 signaling by CD95L presented at this distance $\langle d^* \rangle$ is a universal feature. Hitherto, the discrepancy between different forms of CD95L to induce apoptosis has been based on an earlier study that used a mouse model expressing a constitutively cleaved ligand and lacking the membrane-bound form of CD95L (O' Reilly et al., 2009). They proposed that the observed glomerulonephritis and liver tumors are due to inflammatory functions of circulating sCD95L, as this is not or rarely observed in CD95L mutant *gld* mice (Lynch et al., 1994). However, CD95L-deficient mice do show glomerulonephritis and probably do not develop liver tumors due to their mortality at very young age (Karray et al., 2004). These data can be interpreted differently, as the lower activity of sCD95L might be compensated by a higher production of CD95L that would then be able to reach higher concentrations and delay the symptomatic manifestations compared to CD95L deletion. Along this line, our data highlight that the same cellular responses are elicited by sCD95L and mCD95L but with a much lower activity and slower signal activation in the case of sCD95L.

Moreover, we found that the formation of CD95 clusters scaled with apoptosis induction, where the maximum cluster number was also observed at $\langle d^* \rangle$. To date, the structural information regarding the CD95-CD95L pairs has not been resolved, and yet, the high similarities in the tumor necrosis factor/tumor necrosis factor receptor (TNF/TNFR) family indicate shared properties of ligand-receptor binding (Nagata, 1997; Li et al., 2013). Accordingly, interactions between CD95L and its receptor were assumed to occur in three-to-three mode (Valley et al., 2012). Previous structural studies also unveil a model in which the extracellular ligand/receptor interactions further cooperate with intracellular receptor/FAS-associated death domain protein (FADD)/Caspase-8 interactions through assembly in DD/DD oligomerization. Consequently, the formation of higher order assemblies can initiate CD95 signaling (Siegel et al., 2004; Scott et al., 2009; Wang et al., 2010). In line with this model, we have observed the formation of the large CD95 receptor clusters on mCD95L-supported membranes. A rigid-body-based computational model of membrane receptor-ligand interactions further illustrated that confining the structural flexibility of receptors by membrane topology has an influence on the binding to its ligand (Chen et al., 2017b). Modification of intramolecular flexibility could optimize the binding between ligand and receptors. Indeed, our data show that the anchoring of ligands on membrane surfaces as well as the fine adjustment of inter-ligand distance $\langle d^* \rangle$ have a major influence on the receptor activation, compared to soluble ligands. In addition to the proposed oligomerization models, a growing body of evidence suggests that post-translational modifications (PTMs), particularly glycosylation and palmitoylation, can contribute to the high-order clustering of TNFRs, including CD95, upon ligand activation or at resting pre-ligand state (reviewed in Micheau, 2018; Siegel et al., 2004; Feig et al., 2007). In support of this, the formation of CD95 clusters was found to be dependent on palmitoylation, and the palmitoylated CD95 localized to lipid rafts, as confirmed by photo-activated localization microscopy (PALM) imaging (Cruz et al., 2016).

In addition, the systematic comparison of our results obtained from isolated single cells, tumorspheres *in vitro*, and tumor growth *in vivo* enabled identification of "cell-cell contact" as a major switch of the CD95-mediated cell response from apoptosis to survival. Along this line, in colon epithelial cells, sequestration of CD95 at adherens junctions was shown to inhibit apoptosis through reduced binding capability to CD95L and by formation of a complex with cell polarity molecule Dlg1 that impairs DISC assembly (Gagnoux-Palacios et al., 2018). Our study shows that in addition to inhibition of apoptosis, cell-cell contact facilitates tyrosine phosphorylation of CD95-DD and, thereby, PAC assembly. Similarly, the impact of cell-cell contact on cell-fate decision has been demonstrated in the recent studies. In *Drosophila* pupa, the weakening/loosening of cell contacts leads to a reduction of PIP3 levels, which, in turn, triggers elimination of looser phenotype by apoptosis (Levayer et al., 2015). Additionally, in cancer cells, a switch of cell migration to proliferation occurs by cell-cell contact-mediated vesicular recycling of EGF receptor (EGFR) that leads to the maintenance of ERK activity (Stallaert et al., 2018). Recent studies demonstrate as well that metastatic tumor cells need to be associated in cell clusters together with neutrophils for cell cycle progression (Gkountela et al., 2019; Szczerba et al., 2019), similarly to the correlation of CD95-induced cell divisions and cohesive behavior of cancer cells observed in this study. On a molecular scale, cell-cell contact may energetically favor segregation of proteins or formation of multiprotein complexes, generating domains with a distinct kinase activity, as shown for the T cell receptor (Grakoui et al., 1999; Barthélémy et al., 2000; James and Vale, 2012). Cell-cell contact can provide

spatial cues that coordinate receptor tyrosine kinase (RTK) localization and activity and eventually act as a global regulatory mechanism on cell-cell communication and tissue homeostasis (reviewed in Chiasson-MacKenzie and McClatchey, 2018). Thus, the observed increase in global tyrosine-kinase activity might involve integrins (Aoudjit and Vuori, 2000) and/or RTK-like EGFR (Bivona et al., 2011) that leads to transactivation of CD95. Consistently, EGFR-mediated phosphorylation of CD95 (pY291) leads to proliferation (Ta et al., 2018). Previously, this tyrosine residue (Y291) was found to be susceptible to phosphorylation through members of the Src-family kinases (SFKs), but this modification was considered to be proapoptotic (Atkinson et al., 1996; Gradl et al., 1996). The adaptor proteins and SFK members involved in the interaction with the Y291 at DD of CD95 also differ depending on the cell type. For example, in GBM and NSC cells, PI3K is activated by different SFK members, namely, Yes and c-Src, respectively (Kleber et al., 2008; Corsini et al., 2009; Chakrabandhu and Hueber, 2016), whereas in immune cells, Syk, Fyn, and Lck play a role in SFK-mediated interaction with CD95 (Atkinson et al., 1996; Schlottmann et al., 1996; Letellier et al., 2010). On the other hand, ERK and PI3K are activated in pancreatic cancer cells by adaptor protein Sck (Teodorczyk et al., 2015).

Altogether, our results indicate that the presence of cell-cell contact globally increases tyrosine kinase activity, leading to phosphorylation of the tyrosine residue within the DD of CD95 and final engagement of a survival program. Also, this study highlights how cellular architecture, specifically physical contact with neighboring cells, can fine-tune the cellular response to CD95 activation.

Blocking non-apoptotic functions of CD95 is a promising therapy option for cancer. Accordingly, a phase II clinical trial in glioblastoma patients by using a fusion CD95-FC protein that neutralizes CD95L and, thus, CD95 activity increased the overall survival of patients with the unmethylated-CD95L promoter (Wick et al., 2014). Yet, as reported for previous strategies targeting kinase activities, other receptors might take over, leading to therapy resistance in the long term (Xu and Huang, 2010). Our study unveils a strategy to convert the tumorigenic signal into apoptosis by targeting tyrosine phosphorylation at DD of CD95 and, thereby, avoid the risk of therapy resistance to neutralizing CD95 therapies for cancer patients.

STAR★METHODS

Detailed methods are provided in the online version of this paper and include the following:

SUPPLEMENTAL INFORMATION

Supplemental Information can be found online at https://doi.org/10.1016/j.celrep.2019.10.054.

ACKNOWLEDGMENTS

We thank the Nikon Imaging Center at the University of Heidelberg for providing assistance in their imaging facility. We thank Katrin Volk for technical support. Histology services for tumor pathology analysis were provided by the Institute of Pathology, University Hospital Heidelberg. We thank the DKFZ Mass Spectrometry Core facility for mass spectrometry analysis. This research was supported by German Research Foundation, DFG/Transregio 186 (TRR186) (to A.M.-V.), and DFG/Sonderforschungsbereich 873 (SFB 873) (to A.M.-V. and M.T.). M.T. thanks the Nakatani Foundation for support. C.M. is grateful for the financial support of the Excellence Cluster Cell Networks and Fonds der Chemischen Industrie. This work was funded by the German Cancer Research Center (DKFZ) and the Helmholtz Alliance PCCC (HGF). G.S.G.B. is a member of the Hartmut-Hoffmann Berling International Graduate School of Molecular and Cell Biology of the University of Heidelberg (HBIGS) and Helmholtz International Graduate School (HIGS) of DKFZ.

AUTHOR CONTRIBUTIONS

Acquisition, Analysis, and Interpretation of Experimental Data, G.S.G.B., C.M., S.K., J.B., and T.K.; Inflow Microscopy, E.B. and Y.S.; Endothelial Tube Formation Assay; S.C.; ICAM1 Binding Assay, L.G.; Resources, M. Thiemann and C.R.W.; Writing - Original Draft Preparation, G.S.G.B., A.M.-V., and M. Tanaka; Writing - Review & Editing, J.B., C.M., and S.K.; Conceptualization, A.M.-V. and M. Tanaka; Supervision, A.M.-V., M. Tamala, and Y.S.; Project Design; A.M.-V. and G.S.G.B.; Oversight; A.M.-V.

DECLARATION OF INTERESTS

The authors declare no competing interests.

Received: November 11, 2018
Revised: August 14, 2019
Accepted: October 11, 2019
Published: November 19, 2019

REFERENCES

Alderson, M.R., Tough, T.W., Davis-Smith, T., Braddy, S., Falk, B., Schooley, K.A., Goodwin, R.G., Smith, C.A., Ramsdell, F., and Lynch, D.H. (1995). Fas ligand mediates activation-induced cell death in human T lymphocytes. J. Exp. Med. *181*, 71–77.

Aoudjit, F., and Vuori, K. (2000). Engagement of the alpha2beta1 integrin inhibits Fas ligand expression and activation-induced cell death in T cells in a focal adhesion kinase-dependent manner. Blood *95*, 2044–2051.

Arnaoutova, I., George, J., Kleinman, H.K., and Benton, G. (2009). The endothelial cell tube formation assay on basement membrane turns 20: state of the science and the art. Angiogenesis *12*, 267–274.

Atkinson, E.A., Ostergaard, H., Kane, K., Pinkoski, M.J., Caputo, A., Olszowy, M.W., and Bleackley, R.C. (1996). A physical interaction between the cell death protein Fas and the tyrosine kinase p59fynT. J. Biol. Chem. *271*, 5968–5971.

Barnhart, B.C., Legembre, P., Pietras, E., Bubici, C., Franzoso, G., and Peter, M.E. (2004). CD95 ligand induces motility and invasiveness of apoptosis-resistant tumor cells. EMBO J. *23*, 3175–3185.

Barthélémy, M., Buldyrev, S.V., Havlin, S., and Stanley, H.E. (2000). Multifractal properties of the random resistor network. Phys. Rev. E Stat. Phys. Plasmas Fluids Relat. Interdiscip. Topics *61*, R3283–R3286.

Bivona, T.G., Hieronymus, H., Parker, J., Chang, K., Taron, M., Rosell, R., Moonsamy, P., Dahlman, K., Miller, V.A., Costa, C., et al. (2011). FAS and NF-κB signalling modulate dependence of lung cancers on mutant EGFR. Nature *471*, 523–526.

Brunner, T., Mogil, R.J., LaFace, D., Yoo, N.J., Mahboubi, A., Echeverri, F., Martin, S.J., Force, W.R., Lynch, D.H., Ware, C.F., et al. (1995). Cell-autonomous Fas (CD95)/Fas-ligand interaction mediates activation-induced apoptosis in T-cell hybridomas. Nature *373*, 441–444.

Burk, A.S. (2015). Quantifying adhesion and morphological dynamics of human hematopoietic stem and progenitor cells on novel in vitro models of bone marrow niche. https://katalog.ub.uni-heidelberg.de/cgi-bin/titel.cgi?katkey=67899300&sess=964a6df2ae42bd0084c35c4255dcaf5d&query=si%3A%22451513398%22.

Burk, A.S., Monzel, C., Yoshikawa, H.Y., Wuchter, P., Saffrich, R., Eckstein, V., Tanaka, M., and Ho, A.D. (2015). Quantifying adhesion mechanisms and dynamics of human hematopoietic stem and progenitor cells. Sci. Rep. *5*, 9370.

Chakrabandhu, K., and Hueber, A.-O. (2016). Fas Versatile Signaling and Beyond: Pivotal Role of Tyrosine Phosphorylation in Context-Dependent Signaling and Diseases. Front. Immunol. *7*, 429.

Chakrabandhu, K., Huault, S., Durivault, J., Lang, K., Ta Ngoc, L., Bole, A., Doma, E., Dérijard, B., Gérard, J.P., Pierres, M., and Hueber, A.O. (2016). An Evolution-Guided Analysis Reveals a Multi-Signaling Regulation of Fas by Tyrosine Phosphorylation and its Implication in Human Cancers. PLoS Biol. *14*, e1002401.

Chen, J.J., Sun, Y., and Nabel, G.J. (1998). Regulation of the proinflammatory effects of Fas ligand (CD95L). Science *282*, 1714–1717.

Chen, S., Tisch, N., Kegel, M., Yerbes, R., Hermann, R., Hudalla, H., Zuliani, C., Gülcüler, G.S., Zwadlo, K., von Engelhardt, J., et al. (2017a). CNS Macrophages Control Neurovascular Development via CD95L. Cell Rep. *19*, 1378–1393.

Chen, J., Almo, S.C., and Wu, Y. (2017b). General principles of binding between cell surface receptors and multi-specific ligands: A computational study. PLoS Comput. Biol. *13*, e1005805.

Chiasson-MacKenzie, C., and McClatchey, A.I. (2018). Cell-Cell Contact and Receptor Tyrosine Kinase Signaling. Cold Spring Harb. Perspect. Biol. *10*, a029215.

Monzel, C., and Möhl, C. (2016). Introduction to Matlab. In Bioimage Data Analysis, K. Miura, ed. (Wiley-VCH), pp. 63–97.

Corsini, N.S., Sancho-Martinez, I., Laudenklos, S., Glagow, D., Kumar, S., Letellier, E., Koch, P., Teodorczyk, M., Kleber, S., Klussmann, S., et al. (2009). The death receptor CD95 activates adult neural stem cells for working memory formation and brain repair. Cell Stem Cell *5*, 178–190.

Cruz, A.C., Ramaswamy, M., Ouyang, C., Klebanoff, C.A., Sengupta, P., Yamamoto, T.N., Meylan, F., Thomas, S.K., Richoz, N., Eil, R., et al. (2016). Fas/CD95 prevents autoimmunity independently of lipid raft localization and efficient apoptosis induction. Nat. Commun. *7*, 13895.

Daigle, I., Yousefi, S., Colonna, M., Green, D.R., and Simon, H.U. (2002). Death receptors bind SHP-1 and block cytokine-induced anti-apoptotic signaling in neutrophils. Nat. Med. *8*, 61–67.

Desbarats, J., Birge, R.B., Mimouni-Rongy, M., Weinstein, D.E., Palerme, J.S., and Newell, M.K. (2003). Fas engagement induces neurite growth through ERK activation and p35 upregulation. Nat. Cell Biol. *5*, 118–125.

Dhein, J., Walczak, H., Bäumler, C., Debatin, K.M., and Krammer, P.H. (1995). Autocrine T-cell suicide mediated by APO-1/(Fas/CD95). Nature *373*, 438–441.

Drachsler, M., Kleber, S., Mateos, A., Volk, K., Mohr, N., Chen, S., Cirovic, B., Tüttenberg, J., Gieffers, C., Sykora, J., et al. (2016). CD95 maintains stem cell-like and non-classical EMT programs in primary human glioblastoma cells. Cell Death Dis. *7*, e2209.

Feig, C., Tchikov, V., Schutze, S., and Peter, M.E. (2007). Palmitoylation of CD95 facilitates formation of SDS-stable receptor aggregates that initiate apoptosis signaling. EMBO J *26*, 221–231.

Ferrón, S.R., Andreu-Agullo, C., Mira, H., Sanchez, P., Marques-Torrejon, M.A., and Farinas, I. (2007). A combined ex/in vivo assay to detect effects of exogenously added factors in neural stem cells. Nat. Protoc. *2*, 849–859.

Freiberg, R.A., Spencer, D.M., Choate, K.A., Duh, H.J., Schreiber, S.L., Crabtree, G.R., and Khavari, P.A. (1997). Fas signal transduction triggers either proliferation or apoptosis in human fibroblasts. J. Invest. Dermatol. *108*, 215–219.

Gagnoux-Palacios, L., Awina, H., Audeber, S., Rossin, A., Mondin, M., Borgese, F., Planas-Botey, C., Mettouchi, A., Borg, J.P., and Hueber, A.O. (2018). Cell polarity and adherens junction formation inhibit epithelial Fas cell death receptor signaling. J. Cell Biol. *217*, 3839–3852.

Gao, L., Gülcüler, G.S., Golbach, L., Block, H., Zarbock, A., and Martin-Villalba, A. (2016). Endothelial cell-derived CD95 ligand serves as a chemokine in induction of neutrophil slow rolling and adhesion. eLife *5*, e18542.

Gennis, R.B. (1989). Biomembranes: molecular structure and function (Springer-Verlag).

Giancotti, F.G. (2014). Deregulation of cell signaling in cancer. FEBS Lett. *588*, 2558–2570.

Gkountela, S., Castro-Giner, F., Szczerba, B.M., Vetter, M., Landin, J., Scherrer, R., Krol, I., Scheidmann, M.C., Beisel, C., Stirnimann, C.U., et al. (2019). Circulating Tumor Cell Clustering Shapes DNA Methylation to Enable Metastasis Seeding. Cell *176*, 98–112.e14.

Gradl, G., Grandison, P., Lindridge, E., Wang, Y., Watson, J., and Rudert, F. (1996). The CD95 (Fas/APO-1) receptor is phosphorylatedin vitro andin vivo and constitutively associates with several cellular proteins. Apoptosis *1*, 131–140.

Grakoui, A., Bromley, S.K., Sumen, C., Davis, M.M., Shaw, A.S., Allen, P.M., and Dustin, M.L. (1999). The immunological synapse: a molecular machine controlling T cell activation. Science *285*, 221–227.

Gulbins, E., Hermisson, M., Brenner, B., Grassme, H.U., Linderkamp, O., Dichgans, J., Weller, M., and Lang, F. (1998). Cellular stimulation via CD95 involves activation of phospho-inositide-3-kinase. Pflügers Arch. *435*, 546.

Helm, C.A., Knoll, W., and Israelachvili, J.N. (1991). Measurement of ligand-receptor interactions. Proc. Natl. Acad. Sci. USA *88*, 8169–8173.

James, J.R., and Vale, R.D. (2012). Biophysical mechanism of T-cell receptor triggering in a reconstituted system. Nature *487*, 64–69.

Ju, S.-T., Panka, D.J., Cui, H., Ettinger, R., el-Khatib, M., Sherr, D.H., Stanger, B.Z., and Marshak-Rothstein, A. (1995). Fas(CD95)/FasL interactions required for programmed cell death after T-cell activation. Nature *373*, 444–448.

Kaindl, T., Rieger, H., Kaschel, L.M., Engel, U., Schmaus, A., Sleeman, J., and Tanaka, M. (2012). Spatio-temporal patterns of pancreatic cancer cells expressing CD44 isoforms on supported membranes displaying hyaluronic acid oligomers arrays. PLoS One *7*, e42991.

Karray, S., Kress, C., Cuvellier, S., Hue-Beauvais, C., Damotte, D., Babinet, C., and Lévi-Strauss, M. (2004). Complete loss of Fas ligand gene causes massive lymphoproliferation and early death, indicating a residual activity of gld allele. J. Immunol. *172*, 2118–2125.

Kern, W., and Puotinen, D. (1983). Cleaning solutions based on hydrogen peroxide for use in silicon semiconductor technology. RCA Rev. *31*, 187–206.

Kleber, S., Sancho-Martinez, I., Wiestler, B., Beisel, A., Gieffers, C., Hill, O., Thiemann, M., Mueller, W., Sykora, J., Kuhn, A., et al. (2008). Yes and PI3K bind CD95 to signal invasion of glioblastoma. Cancer Cell *13*, 235–248.

Legembre, P., Barnhart, B.C., Zheng, L., Vijayan, S., Straus, S.E., Puck, J., Dale, J.K., Lenardo, M., and Peter, M.E. (2004). Induction of apoptosis and activation of NF-kappaB by CD95 require different signalling thresholds. EMBO Rep. *5*, 1084–1089.

Letellier, E., Kumar, S., Sancho-Martinez, I., Krauth, S., Funke-Kaiser, A., Laudenklos, S., Konecki, K., Klussmann, S., Corsini, N.S., Kleber, S., et al. (2010). CD95-ligand on peripheral myeloid cells activates Syk kinase to trigger their recruitment to the inflammatory site. Immunity *32*, 240–252.

Levayer, R., Hauert, B., and Moreno, E. (2015). Cell mixing induced by myc is required for competitive tissue invasion and destruction. Nature *524*, 476–480.

Li, J., Yin, Q., and Wu, H. (2013). Structural basis of signal transduction in the TNF receptor superfamily. Adv. Immunol. *119*, 135–153.

Lipowsky, R., and Sackmann, E. (1995). Structure and dynamics of membranes. (Elsevier Science).

Lynch, D.H., Watson, M.L., Alderson, M.R., Baum, P.R., Miller, R.E., Tough, T., Gibson, M., Davis-Smith, T., Smith, C.A., Hunter, K., et al. (1994). The mouse Fas-ligand gene is mutated in gld mice and is part of a TNF family gene cluster. Immunity *1*, 131–136.

Martin-Villalba, A., Llorens-Bobadilla, E., and Wollny, D. (2013). CD95 in cancer: tool or target? Trends Mol. Med. *19*, 329–335.

Micheau, O. (2018). Regulation of TNF-Related Apoptosis-Inducing Ligand Signaling by Glycosylation. Int. J. Mol. Sci. *19*, E715.

Nagata, S. (1997). Apoptosis by death factor. Cell *88*, 355–365.

O' Reilly, L.A., Tai, L., Lee, L., Kruse, E.A., Grabow, S., Fairlie, W.D., Haynes, N.M., Tarlinton, D.M., Zhang, J.G., Belz, G.T., et al. (2009). Membrane-bound Fas ligand only is essential for Fas-induced apoptosis. Nature *461*, 659–663.

Sancho-Martinez, I., and Martin-Villalba, A. (2009). Tyrosine phosphorylation and CD95: A FAScinating switch. Cell Cycle *8*, 838–842.

Schlottmann, K.E., Gulbins, E., Lau, S.M., and Coggeshall, K.M. (1996). Activation of Src-family tyrosine kinases during Fas-induced apoptosis. J. Leukoc. Biol. *60*, 546–554.

Schneider, P., Holler, N., Bodmer, J.L., Hahne, M., Frei, K., Fontana, A., and Tschopp, J. (1998). Conversion of membrane-bound Fas(CD95) ligand to its soluble form is associated with downregulation of its proapoptotic activity and loss of liver toxicity. J. Exp. Med. *187*, 1205–1213.

Scott, F.L., Stec, B., Pop, C., Dobaczewska, M.K., Lee, J.J., Monosov, E., Robinson, H., Salvesen, G.S., Schwarzenbacher, R., and Riedl, S.J. (2009). The Fas-FADD death domain complex structure unravels signalling by receptor clustering. Nature *457*, 1019–1022.

Sever, R., and Brugge, J.S. (2015). Signal transduction in cancer. Cold Spring Harb. Perspect. Med. *5*, a006098.

Siegel, R.M., Muppidi, J.R., Sarker, M., Lobito, A., Jen, M., Martin, D., Straus, S.E., and Lenardo, M.J. (2004). SPOTS: signaling protein oligomeric transduction structures are early mediators of death receptor-induced apoptosis at the plasma membrane. J. Cell Biol. *167*, 735–744.

Stallaert, W., Brüggemann, Y., Sabet, O., Baak, L., Battiglio, M., and Bastiaens, P.I.H. (2018). Contact inhibitory Eph signaling suppresses EGF-promoted cell migration by decoupling EGFR activity from vesicular recycling. Sci. Signal. *11*, eaat0114.

Suda, T., Hasimoto, H., Tanaka, M., Ochi, T., and Nagata, S. (1997). Membrane Fas ligand kills human peripheral blood T lymphocytes, and soluble Fas ligand blocks the killing. J. Exp. Med. *186*, 2045–2050.

Szczerba, B.M., Castro-Giner, F., Vetter, M., Krol, I., Gkountela, S., Landin, J., Scheidmann, M.C., Donato, C., Scherrer, R., Singer, J., et al. (2019). Neutrophils escort circulating tumour cells to enable cell cycle progression. Nature *566*, 553–557.

Ta, N.L., Chakrabandhu, K., Huault, S., and Hueber, A.O. (2018). The tyrosine phosphorylated pro-survival form of Fas intensifies the EGF-induced signal in colorectal cancer cells through the nuclear EGFR/STAT3-mediated pathway. Sci. Rep. *8*, 12424.

Tanaka, M., and Sackmann, E. (2005). Polymer-supported membranes as models of the cell surface. Nature *437*, 656–663.

Tanaka, M., Suda, T., Takahashi, T., and Hagata, S. (1995). Expression of the functional soluble form of human fas ligand in activated lymphocytes. EMBO J. *14*, 1129–1135.

Teodorczyk, M., Kleber, S., Wollny, D., Sefrin, J.P., Aykut, B., Mateos, A., Herhaus, P., Sancho-Martinez, I., Hill, O., Gieffers, C., et al. (2015). CD95 promotes metastatic spread via Sck in pancreatic ductal adenocarcinoma. Cell Death Differ. *22*, 1192–1202.

Valley, C.C., Lewis, A.K., Mudaliar, D.J., Perlmutter, J.D., Braun, A.R., Karim, C.B., Thomas, D.D., Brody, J.R., and Sachs, J.N. (2012). Tumor Necrosis Factor-related Apoptosis-inducing Ligand (TRAIL) Induces Death Receptor 5 Networks That Are Highly Organized. J. Biol. Chem. *287*, 21265–21278.

Wang, L., Yang, J.K., Kabaleeswaran, V., Rice, A.J., Cruz, A.C., Park, A.Y., Yin, Q., Damko, E., Jang, S.B., Raunser, S., et al. (2010). The Fas-FADD death domain complex structure reveals the basis of DISC assembly and disease mutations. Nat. Struct. Mol. Biol. *17*, 1324–1329.

Wick, W., Fricke, H., Junge, K., Kobyakov, G., Martens, T., Heese, O., Wiestler, B., Schliesser, M.G., von Deimling, A., Pichler, J., et al. (2014). A phase II, randomized, study of weekly APG101+reirradiation versus reirradiation in progressive glioblastoma. Clin. Cancer Res. *20*, 6304–6313.

Xu, A.M., and Huang, P.H. (2010). Receptor tyrosine kinase coactivation networks in cancer. Cancer Res. *70*, 3857–3860.

Zuliani, C., Kleber, S., Klussmann, S., Wenger, T., Kenzelmann, M., Schreglmann, N., Martinez, A., del Rio, J.A., Soriano, E., Vodrazka, P., et al. (2006). Control of neuronal branching by the death receptor CD95 (Fas/Apo-1). Cell Death Differ. *13*, 31–40.

STAR★METHODS

KEY RESOURCES TABLE

REAGENT or RESOURCE	SOURCE	IDENTIFIER
Antibodies		
Anti-human CD95 (αApo-1)	Apogenix GmbH, Germany	N/A
Goat-anti-mouse phycoerythrin-conjugated	Dianova, Germany	Cat# 115-116-071; RRID: AB_2338626
Anti-human IgG1 phycoerythrin-conjugated	Southern Biotechnology, USA	Cat# 9054-09; RRID: AB_2796628
Anti-CD11b	Novus, USA	Cat# NB110-89474; RRID: AB_1216361
Anti-phospho-ERK	Cell Signaling Technology, Germany	Cat# 4370; RRID: AB_2315112
Anti-phospho-AKT Ser 473	Cell Signaling Technology, Germany	Cat# 9271; RRID: AB_329825
Anti-cleaved-Caspase-3	Cell Signaling Technology, Germany	Cat# 9661; RRID: AB_2341188
Anti-human-Ki67	Novus, USA	Cat# NB600-1252; RRID: AB_2142376
Anti-phospho-Histone 3 (immunohistochemistry)	Millipore/Merck, Germany	Cat# 06-570; RRID: AB_310177
Anti-Pan-Phosphotyrosine	Millipore/Merck, Germany	Cat# 05-321; RRID: AB_309678
Anti-Pan-Phosphotyrosine phycoerythrin-conjugated	Millipore/Merck, Germany	Cat# FCMAB323PE; RRID: AB_10805942
Histone H3 (Western Blot)	Cell Signaling Technology, Germany	Cat# 9717; RRID: AB_331222
Bacterial and Virus Strains		
Lentiviral vector CMV-pEIGW-CD95-Ires-GFP	Martin-Villalba lab	N/A
Lentiviral vector CMV-pEIGW-CD95Y291A-Ires-GFP	Martin-Villalba lab	N/A
pMD2.G VSV G helper plasmid Lentivirus	Trono lab (personal communication)	Addgene #12259
PsPAX2 helper plasmid Lentivirus	Trono lab (personal communication)	Addgene #12260
Lentiviral vector CMV-pEIGW-CD95-YFP	Martin-Villalba lab	N/A
Biological Samples		
Human tumor biopsies from glioblastoma patients	University Hospitals, Mannheim, Charité Berlin and Ulm/Günzburg, Germany	N/A
Human tumor biopsies from Pancreatic ductal adenocarcinoma patients	University Hospital Heidelberg, Germany	N/A
Chemicals, Peptides, and Recombinant Proteins		
1,2-dioleoyl-*sn*-glycero-3-phosphocholine (DOPC)	Avanti Polar Lipids, USA	#850375C
18:1 Biotinyl Cap PE (biotin-DOPE)	Avanti Polar Lipids, USA	#870273C
1,2-dipalmitoyl-*sn*-glycero-3-phosphocholine (DPPC)	Avanti Polar Lipids, USA	#850355C
Neutravidin (deglycosylatedavidin)	Life Technologies, Germany	#A-2666
Phalloidin-Alexa 488	Thermo Fisher, USA	#12379
Recombinant human EGF	Promocell	#C-60170
Recombinant basic FGF	Pelobiotech, Germany	#PB-ZAF3007-50
NH_4OH	Sigma Aldrich, USA	#13360
Triton X-100	Sigma Aldrich, USA	#x100-100ml
Saponin	Sigma Aldrich, USA	#S4521-10G
Bovine Serum Albumin	Sigma Aldrich, USA	#05479-50G
Recombinant Human ICAM-1/CD54 Fc	R&D systems, USA	#796-IC-050
Polydimethylsiloxane	Dow Corning Co., USA	
Chloroform	Sigma Aldrich, USA	#C2432-500ML
Roti-Histofix 4%	Carl Roth, Germany	#P087.1
Fluoromount-G	Biozol, Germany	#0100-01
Calcein AM, Live cell dye	Life Technologies, Germany	#C34852
Proteinase inhibitor Cocktail Complete	Roche	#11697498001
Sodium Ortho Vanadate	Sigma Aldrich, USA	#S-6508

(*Continued on next page*)

Continued

REAGENT or RESOURCE	SOURCE	IDENTIFIER
Phosphatase Inhibitor Cocktail	Cell Signaling Technology, USA	#5870S
Pierce IP Lysis Buffer	Pierce/Thermo Fisher, USA	#87788
Hoechst 33342	Biotrend, Germany	#40047
Gelatin solution	Sigma Aldrich, USA	#G1393-100 ml
Biotinylated human CD95L trimer (CD95L-T4-btn)	Apogenix GmbH, Germany	N/A
Critical Commercial Assays		
QIFIKIT (measures average amount of CD95 receptors on cell surfaces)	Dako, Germany	#K007811
EGM-2 SingleQuot Kit (Supplements and Growth Factors for endothelial cells	Lonza, USA	#CC-4176
Experimental Models: Cell Lines		
Human derived primary Glioblastoma cells (GBM)	University Hospitals Mannheim, Berlin (Charité) and Ulm/Günzburg, cultured in the laboratory of Ana Martin-Villalba, DKFZ, Heidelberg	N/A
Human derived primary Pancreatic ductal adenocarcinoma cells (PanD24)	University Hospital Heidelberg, cultured in the Laboratory of Ana Martin-Villalba, DKFZ, Germany	N/A
Spontaneous murine Astrocytoma-560 (SMA-560)	Laboratory of Anne Regnier-Vigouroux, DKFZ, Germany	N/A
Murine primary Neutrophils	Laboratory of Ana Martin-Villalba, DKFZ, Germany	N/A
Human endothelial cells (HUVEC)	Lonza, USA	#C2519A
Experimental Models: Organisms/Strains		
Mouse/VMDK	Central animal facility at DKFZ, Germany	N/A
Mouse/CB17-SCID (CB17.Cg -*Prkdc*^{scid}*Lyst*$^{bg\text{-}J}$/Crl)	Charles River	Strain Code:250
C57BL/6J	Charles River	Strain Code:027
Software and Algorithms		
ImageJ/Fiji	NIH, USA	https://imagej.nih.gov/ij/download.html
Cell Quest Software	Becton Dickinson, Germany	N/A
IDEAS 6.0 Software	Amnis/Millipore, USA	N/A
Mascot Software	Matrix Science, USA	N/A
MATLAB	MathWorks	N/A
Other		
Dulbecos Modified Eagle Medium (DMEM):HAM's nutrient mixture F12	Thermo Fisher, USA	#21331-020
Neurobasal Medium A	Life Technologies, Germany	#10888022
RPMI 1640 Medium	Life Technologies, Germany	#21875-034
Hanks Balanced Salt Solution (HBSS)	Life Technologies, Germany	#14170138
Endothelial basal Medium-2 (EBM-2)	Lonza, USA	#CC-3156
B27 Supplement	Life Technologies, Germany	#17504044
N2-Supplements	Life Technologies, Germany	#17502048
L-Glutamine	Life Technologies, Germany	#25030024
Heparin	Sigma Aldrich, USA	#H3149-100KU
Accutase	Thermo Fisher, USA	#A6964
Trypsin-EDTA	Life Technologies, Germany	#25300096
Plastic fluidic channels μ-Slide VI$^{0.4}$	IBIDI, Germany	#80608
Glass slides	Menzel GmbH, Germany	#BB024060A1

(*Continued on next page*)

Continued

REAGENT or RESOURCE	SOURCE	IDENTIFIER
Penicillin and streptomycin	Thermo Fisher, USA	#15140-122
Porous silica microspheres (NUCLEOSIL® 100-10C_{18}) (10 μm)	Macherey-Nagel, Germany	#712150.10
De-ionized ultrapure water	Genpure, TKA, Germany	#50131256

LEAD CONTACT AND MATERIALS AVAILABILITY

Further information and requests for mouse strains, resources, and reagents should be directed to and will be fulfilled by the Lead Contact, Ana Martin-Villalba at a.martin-villalba@dkfz-heidelberg.de. This study did not generate other new unique reagents.

EXPERIMENTAL MODEL AND SUBJECT DETAILS

Animal Studies

C57BL/6J WT and CB.17$^{SCID/bg}$ mice were purchased from Charles River. VMDK mice were bred by the in-house animal facility German Cancer Research Center (DKFZ). Littermate controls were used where appropriate. Mice were maintained in specific pathogen-free animal facilities at German Cancer Research Center (DKFZ) (Heidelberg, Germany). All animal experiments were performed in accordance with the institutional guidelines of the German Cancer Research Center and were approved by the Regierungspräsidium Karlsruhe, Germany.

For subcutaneous injection of tumor cells and i.v. injection of coated beads, CB.17$^{SCID/bg}$ mice (8 −10 weeks old, female) were subcutaneously transplanted with 10000 GBM cells in 100 μl matrigel. Tumor size was measured every week with a caliper and after establishment of tumors, mice were intravenously injected with 2 × 10^6 DOPC or 1% beads through the tail vein. Two weeks later animals were sacrificed and tumors were retrieved after transcardial perfusion.

For, orthotopic injection of tumor cells and coated beads, SMA-560 tumor cells were transplanted into 8 to 10 week old, female VMDK mice (in house breeding). Therefore, 5000 tumor cells were re-suspended in 2 μl of Hanks buffered saline solution (HBSS) and loaded into a 10 μl nanofill syringe (WPI) and stereotactically injected into the striatum (2.5 mm lateral of the bregma to a depth of 3 mm) of isofluorane-anaesthetized mice. Five days post-injection 2 × 10^6 control beads (DOPC) or CD95L-coated beads (1% Beads) were inoculated at exactly the same position as the tumor cells before. On reaching the no-go criteria, which are declined in the animal permission, mice were sacrificed and brains were retrieved after transcardial perfusion.

For perfusion, mice were anesthetized by intraperitoneal injection of 800 μl perfusion solution. After the thoracic cavity was opened, the heart was exposed and transcardial perfusion was performed with 10 mL HBSS. For immunohistochemistry, the mice were additionally perfused with 10 mL of 4% PFA.

Cell Culture

Collection of patient samples was approved by the Ethics committees of the Charité University Medicine, Campus Virchow-Klinikum, Berlin (EA3/023/06) and Heidelberg University, Medical Faculty (S-233/2016). The information of the age/sex of patients is not available with regard to patient privacy protection. The specimen was examined by a neuropathologist to confirm that the tumor met WHO criteria for glioblastoma. The sample was dissociated using the Brain Tumor Dissociation Kit (P) (MiltenyiBiotec GmbH, Bergisch-Gladbach, Germany) and subsequently expanded in Neurobasal medium supplemented with B27 (2 vol.%), 2 mM L-glutamine, heparin (2 μg/ml), EGF (20 ng/ml) and bFGF (20 ng/ml) at 5% CO_2 and 37°C.

Glioblastoma multiforme (GBM) stem cells were established from mechanically and enzymatically dissociated brain tumor samples (GBM6, GBM10, GBM39, GBM50, GBM60). The cells were cultured in serum-free medium containing stem-cell mitogens as mentioned above. Prior to experiments, the agglomerated cells were centrifuged and re-suspended with Accutase (ThermoFisher) to get a single cell suspension, which was further diluted in freshly prepared cell culture medium to concentrations of ~2 × 10^5 cells/ml.

SMA-560 and HeLa cells were maintained in DMEM supplemented with 10% fetal calf serum, 1 x glutamine and 1 x penicillin/streptomycin. Cells were kept in 5% CO_2 at 37°C.

METHOD DETAILS

Preparation of Supported Membranes

Before the assembly of sample chambers, glass substrates were cleaned by a modified RCA protocol (Kern and Puotinen, 1983): briefly, samples were sonicated for 5 min in acetone, ethanol, methanol, and water, then immersed in a solution of H_2O_2 (30%) / NH_4OH (30%) / H_2O (1:1:5 by volume) and sonicated for 5 min at room temperature before soaking them for another 30 min at 60°C. Afterward, glass substrates were intensively rinsed with water, dried at 70°C, and stored in a vacuum chamber.

Sample chambers were individually assembled by bonding the cleaned glass slides (25 × 75 mm, Menzel GmbH, Braunschweig, Germany) to plastic fluidic channels (μ-slide VI, ibidi, Munich, Germany). Polydimethylsiloxane produced from base and curing agent (SYLGARD184, Dow Corning Co., USA) served as bonding agent.

Supported membranes were prepared by drying stock solutions of either DOPC or DPPC containing 0.2, 0.5, 0.8, 1.0 and 1.5 mol % biotin-DOPE in chloroform in a nitrogen stream. Dried samples were kept in a vacuum chamber at 25°C for 12 h, and were re-suspended in de-ionized water to a concentration of ~1 mg/ml. Small unilamellar vesicles (SUVs) were prepared by pulsed sonication of the lipid solution using a tip sonicator (Misonix, New York, USA) for 30 min at 1.0 W. Subsequently, SUV suspensions were incubated on the cleaned, bonded sample chambers where they formed a lipid bilayer on the glass surface. After 45 min. of incubation, the chambers were intensively rinsed with de-ionized water to remove remaining SUVs. Subsequently, the supported membranes were incubated with 1 μg/ml neutravidin solution for 30 min and were thoroughly washed with de-ionized water. Next, the membranes were incubated with aqueous CD95L-T4-btn (2 μg/ml) solution for 1 h at room temperature. Finally, the samples were carefully washed with pre-warmed cell culture medium and kept at 37°C prior to cell experiments.

CD95L-Containing Supported Membrane on Silica Beads

SUVs prepared as described above were used to form supported membrane on porous silica microspheres (NUCLEOSIL® standard C18 phases, nonpolar from Macherey-Nagel, Düren, Germany). Lipid vesicles were incubated with silica beads at 60°C for 2 h under rotation. The lipid-coated beads were collected by centrifugation and washed with PBS. CD95L functionalization of the supported membrane on the beads was performed as described above. Here, the beads were kept on a shaker during each incubation step.

Cell Imaging

Cell death was measured by microscopy using transmitted light imaging and cell morphology analysis. Images were taken on a Leica SP5 confocal microscope (Leica Microsystems, Mannheim, Germany) or on an OlympusCKX41 wide-field microscope equipped with an Olympus PEN Lite CCD camera (Olympus Europa, Hamburg, Germany). Cell death kinetics were quantified from images taken every 10 min and by manually marking the first rounding and shrinkage event due to cell death. Marks were then automatically segmented and counted in ImageJ.

To obtain statistically reliable data, we collected results from 3 independent measurements for each experimental condition. For every single experiment, cellular concentration of 10^6/ml were plated per channel of the 6 channel chambers. The total number of cells was counted from 5 - 8 phase contrast images. Time-lapse images were recorded on a fully automated Leica SP5 confocal microscope (Leica Microsystems, Mannheim, Germany) equipped with an Apo 63 x NA 1.4 oil immersion objective using a proprietary macro for auto-focusing and multi-position imaging.

The microscope stage was maintained at 37°C and CO2 at 5%. Apoptotic cells were identified by monitoring irreversible cell blebbing and fragmentation of cell nuclei. The area of cell adhesion and CD95-GFP clusters were detected by morphological identification and intensity threshold. Images were analyzed using ImageJ/Fiji (NIH,USA) as well as routines written in MATLAB (R2013b, The Math Works Inc, MA, USA) following cell segmentation scripts (Monzel and Möhl, 2016).

Lentiviral Transductions

For PanD24, cells were infected with lentiviral vector pEIGW-CD95-YFP at a multiplicity of infection (MOI) of 5. Expression of all transgenes was confirmed in infected cells by FACS analysis of YFP expression.

For lentiviral infections, GBM cells were sorted for CD95 negative surface expression ($CD95^{neg}$ cells). $CD95^{neg}$ cells were infected with the lentiviral vector pEIGW-CD95-Tyr (Y291) or pEIGW-CD95-Ala (A291) at a multiplicity of infection (MOI) of 5. The plasmids were constructed by site directed mutagenesis to exchange the tyrosine residue (Y291) to alanine in the DD of CD95 in pEIGW-CD95-Tyr. All lentiviruses were propagated using previously described methods (Zuliani et al., 2006). Expression of all transgenes was confirmed in infected cells by FACS analysis of GFP expression. The percentage of infected cells was 60%–80%. The GFP positive cells were sorted according to their expression level and expanded for further experiments.

Quantification of CD95 Receptor Levels Presented on the Cell Surface

For the comparison of adhesion/apoptosis behaviors between different cells, the average amount of CD95receptors expressed on each cell type was calculated by FACS analysis using QIFIKIT (Dako) according to manufacturer's protocol. Briefly, a calibration curve was constructed using calibration beads followed by determination of CD95 molecules on the cell surface. For CD95 staining, αApo-1 (Apogenix, 0.01 μg/μl) was incubated for 20 min on ice, followed by incubation of the secondary antibody (1:30 goat-anti-mouse phycoerythrin-conjugated; Dianova) for 30 min. Flow cytometry analysis was performed on a FACS Calibur (Becton Dickinson) using Cell Quest Software. The surface area of PanD24 and GBM cells was calculated from the projected diameter of non-adherent cells obtained from phase contrast images.

Immunohistochemistry of the Brain

For immunohistochemistry of the tumor bearing brains, mice were sacrificed as described above and brains were extracted and fixed in 4% PFA overnight. 100 μm coronal sections were prepared using a vibratome (Leica, Germany). Sections were stored in PBS with 0.05% sodium azide until staining. For the staining, sections were incubated in PBS with 0.3% Triton X-100 and 5% horse serum for

one h to block unspecific binding sites. For different analyses, sections were stained with anti-phospho ERK (1:200; CST), anti-phospho Ser 473 Akt (1:25; CST), anti-cleaved Caspase-3 (1:100; CST), anti-Ki67 (1:200; Novus) and anti-pH3 (1:1000; Millipore) antibody diluted in blocking solution for 72 h at 4°C with shaking. After washing the sections 3 times for 5 min each with PBS, secondary antibody staining was performed using the appropriate Alexa-fluorophore antibodies diluted in blocking buffer for 2 h at room temperature. Furthermore, Hoechst33342 was added to the secondary antibody dilution to stain for nuclei. Sections were then washed three times for 5 min with PBS, and in a last step with PB (Phosphate buffer without salt) buffer. After mounting with Fluoromount-G, the sections were allowed to dry at room temperature for overnight and were stored in the dark at 4°C until imaging.

Sphere Formation Assay

Neurosphere assays were performed as previously described with slight modifications (Ferrón et al., 2007). In brief, tumorspheres were harvested 3 to 7 days after culturing by centrifugation and dissociated using Accutase (ThermoFisher), thereafter cells were centrifuged and Accutase was replaced by normal Neurobasal medium. The cell suspension was counted and 2×10^5 cells per well were cultured on a 6 well plate. The next day, the newly formed spheres were collected by centrifugation, resuspended in 100 μl of Neurobasal medium and were incubated for 4 h with either the ligand coated membrane or the control DOPC membrane. Afterward the cells were harvested and centrifuged, and the cell pellet was shortly treated with Accutase to obtain a single cell suspension. For the sphere formation assay 500 cells/well were seeded in a 96 well plate. From each condition 10 wells were plated and analyzed. The number of tumorspheres per well was scored by microscopic examination 10 days after seeding.

Endothelial Tube Formation Assay

HUVECs (Lonza) were maintained in endothelial basal medium-2 (EBM-2, Lonza) supplemented with EGM-2 SingleQuot Kit Supplements and Growth Factors (Lonza) on 0.1% gelatin-coated flasks. The endothelial tube formation assay was performed according to Arnaoutova et al., (2009). 80 μl of growth factor reduced matrigel was plated in each well of a 96-well plate and allowed to gel at 37°C for 30 min. 15000 HUVECS in EBM-2 supplemented with 35 ng/μl bFGF were seeded per well and the formation of endothelial tubes was assessed after 12 hours. For visualization, tubes were stained with the live cell dye Calcein AM (8 μg/ml) before imaging. Experiments were performed in triplicates.

For CD95L stimulation, HUVECs were stimulated for 4 hours on control- or mCD95L- supported membranes prior to plating on matrigel.

Soluble ICAM1 Binding Assay

Culture of mouse bone marrow-derived neutrophils and soluble ICAM1 binding assay was performed as previously described (Gao et al., 2016). Neutrophils were cultivated in RPMI (2% FCS) for 4 hours before stimulation. Subsequently, the cells were suspended in Hanks Balanced Salt Solution containing 1 mM CaCl2 and MgCl2. Next, the cell suspension was stimulated on mCD95L membranes or on DOPC membranes in the presence of ICAM1/FC (20 mg/ml, R&D systems, USA) and PE-conjugated anti-human IgG1 (Fc-specific; Southern Biotechnology, USA) for 10 min at 37°C. Anti-CD11b (10 mg/ml) antibody was used to block the Mac-1-dependent ICAM1 binding. The binding of ICAM1 was determined by flow cytometry.

pTyr-Western Blot Analysis of Single Cells and Spheres

GBM cells were dissociated by Accutase treatment for 4 min one day before the experiment and plated as 5×10^5 cells per well into 6-well plate. Next day, cells in one well was dissociated by Accutase and plated into 10 cm plate for 1 h recovery. Thereafter, the cells in the 10 cm plate were used as single cell sample and the cells taken from 6-well plate were used as sphere sample. The samples were then collected and lysed for western blot analysis against generic pTyr (4G10, Millipore) antibody.

Inflow Microscopy

GBM cells were dissociated by Accutase treatment for 4 min and 5×10^5 cells were plated into 10 cm plate for 3 h. For pTyr control samples, cells were either treated with EGF (100 ng/ml, 10 min) or vanadate (1 mM, 30 min) after cell dissociation and plating for 3 h. Thereafter, the cells were collected and fixed with paraformaldehyde (1.5%) for 10 min at RT. Consequently, cells were permeabilized with saponin (0.1%) for 20 min and stained with the following antibody and fluorescent dye mixture in blocking buffer (1% BSA in PBS) for 30 min; DAPI (Sigma; 1:10000), pTyr-PE (4G10, Millipore; 1:15), Phalloidin-Alexa fluorophore 488 (Thermo Fischer; 1:800). Thereafter, cells were washed and resuspended in PBS. Finally, samples were subjected to Inflow microscopy (ImageStream®X) and 10,000-20,000 cells per sample were acquired using 60 x objective.

Analysis of phalloidin and pTyr signal intensities in singlets versus doublets was performed using IDEAS 6.0 software. Briefly, cells that were out of focus were gated out using the "Gradient RMS" feature. Next, singlets and potential doublets were gated using area (Area_M07) and intensity (Intensity_MC_Ch7) features based on the nuclei staining. After that, the real doublets were further gated using the "Aspect Ratio Intensity_M01_Ch01" and "Area_M01" features. Aspect ratio is the minor axis intensity divided by major axis intensity based on the brightfield intensity of the samples. In the final step, mean pixel intensity and mean fluorescent intensity (total intensity) of the respective signals were automatically calculated in the singlet and doublet populations.

Phosphotyrosine Immunoprecipitation and LC-MS/MS Analysis

The magnetic beads conjugated with anti-phosphotyrosine (Millipore) were used to immunoprecipitate (IP) tyrosine phosphoproteins from GBM6 CD95 wild-type (CD95wt) or GBM6 CD95 Alanine mutant (CD95Ala) cells that were stimulated with Apo-1 (Apogenix) for 5 min prior to IP. Briefly, 1 mg of cell lysate was incubated with magnetic beads overnight at 4°C by rotation. Beads were washed extensively in lysis buffer (Pierce IP lysis buffer) with inhibitors (cOmplete protease inhibitor cocktail, vanadate and phosphatase inhibitor cocktail) and boiled to elute enriched tyrosine phosphoproteins from beads. The IP samples and flow-through (FT) were subjected to MS/MS analysis. After Coomassie staining, region of interest corresponding to the size of CD95 (40 - 50 kDa) were excised from gel and subjected to in-gel digestion with trypsin. Samples were analyzed by LC-MS/MS using nanoflow-HPLC system interfaced to electrospray Q-TOF tandem mass spectrometers. Protein identification via peptide MS/MS spectra was achieved by using the Mascot software for searching the NCBI non-redundant protein database.

QUANTIFICATION AND STATISTICAL ANALYSIS

The statistical data reported in this study include results from at least three biological replicates, except for MS analysis. All statistical analyses were performed in GraphPad Prism Version 5 (GraphPad Software) and expressed as mean ± standard error of the mean (SEM). Statistical significance was determined using one-way ANOVA for multiple comparisons, or two-tailed paired Student's t test when applied to two independent groups, * $p < 0.05$, ** $p < 0.01$, and *** $p < 0.001$.

Calculation of Intermolecular Distance ⟨d⟩

The intermolecular distance ⟨d⟩ between the ligand molecules on the membrane surface was controlled by adjusting the fraction χ_{biotin} of the lipids functionalized with biotin anchors (DOPE-biotin). As we reported in previous accounts (Burk et al., 2015; Kaindl et al., 2012), DOPE-biotin lipids are uniformly mixed with matrix lipids as monomers and thus the intermolecular distance between the DOPE-biotin can be calculated from the area per lipid molecule A ≈ 0.6 nm^2 (Lipowsky and Sackmann, 1995) as:

$$\langle d \rangle \approx \sqrt{0.6/\chi_{biotin}}\ [\mathrm{nm}].$$

Considering the extremely high affinity of biotin-neutravidin crosslinkers ($k_D \sim 10^{-15}$ M) (Helm et al., 1991), quartz crystal microbalance data demonstrated that the binding stoichiometry of biotin-DOPE and biotinylated protein is 1:1 after ≈300 min (Burk, 2015). The density ρ of CD95L on the membrane corresponds to:

$$\chi = \chi_{max} - \frac{\chi_{max} - \chi_{min}}{1 + \left(\frac{t}{t_{half}}\right)^n}$$

Hill Equation

The number of apoptotic cells over time followed a sigmoid curve, which was fitted with a Hill-equation (solid lines) to characterize the dynamics of the cellular response:

The Hill equation was used as an empirical indicator to judge the cooperativity of the reaction as a function of time t :

$$\chi = \chi_{max} - \frac{\chi_{max} - \chi_{min}}{1 + \left(\frac{t}{t_{half}}\right)^n} \qquad \text{(Eq. 1)}$$

where χ_{max} and χ_{min} are the maximum and minimum level of the fraction of cells adherent to the surface χ. t_{half} is the time after which half of the apoptotic cells have died. Its value is reported in Tables S2 and S4 as "half-time." The cooperativity coefficient (Hill coefficient) adopted values from ~1 to 6 indicating the necessity of neighboring CD95L to diffuse to the optimal confinement, before the signal is transduced. In case of the optimal distance $\langle d^* \rangle$, the cooperativity coefficient is the lowest, $n \approx 1$, because the reaction immediately takes place with no lag time. This is a quantitative indication that the pre-confinement of CD95L molecules has a major impact on the reaction kinetics.

DATA AND CODE AVAILABILITY

The raw data supporting the current study are available from the Lead Contacts upon request. All software is commercially available.